MICROCOPY RESOLUTION TEST CHART
NATIONAL BUREAU OF STANDARDS-1963-A

LEVEL

AD-E300 551

DNA 4188F

A REVIEW OF EARTH PENETRATING WEAPON CALCULATIONS

R.L. Bjork

Pacifica Technology

P.O. Box 148

Del Mar, California 92014

31 December 1975

CONTRACT No. DNA 001-75-C-0148

APPROVED FOR PUBLIC RELEASE;
DISTRIBUTION UNLIMITED.

Prepared for

Director

DEFENSE NUCLEAR AGENCY

Washington, D. C. 20305

79 06 08 01

Destroy this report when it is no longer
needed. Do not return to sender.

PLEASE NOTIFY THE DEFENSE NUCLEAR AGENCY,
ATTN: TISI, WASHINGTON, D.C. 20305, IF
YOUR ADDRESS IS INCORRECT, IF YOU WISH TO
BE DELETED FROM THE DISTRIBUTION LIST, OR
IF THE ADDRESSEE IS NO LONGER EMPLOYED BY
YOUR ORGANIZATION.

REPORT DOCUMENTATION PAGE		READ INSTRUCTIONS BEFORE COMPLETING FORM
1. REPORT NUMBER DNA 4188F	2. GOVT ACCESSION NO.	3. RECIPIENT'S CATALOG NUMBER
4. TITLE (and Subtitle) A REVIEW OF EARTH PENETRATING WEAPON CALCULATIONS		5. TYPE OF REPORT & PERIOD COVERED Final Report for Period 3 Dec 74—31 Dec 75
		6. PERFORMING ORG. REPORT NUMBER PT-U75-0013
7. AUTHOR(s) R. L. Bjork		8. CONTRACT OR GRANT NUMBER(s) DNA 001-75-C-0148
9. PERFORMING ORGANIZATION NAME AND ADDRESS Pacifica Technology P.O. Box 148 Del Mar, California 92014		10. PROGRAM ELEMENT, PROJECT, TASK AREA & WORK UNIT NUMBERS NWED Subtask Y99QAXSB048-02
11. CONTROLLING OFFICE NAME AND ADDRESS Director Defense Nuclear Agency Washington, D.C. 20305		12. REPORT DATE 31 December 1975
		13. NUMBER OF PAGES 70
14. MONITORING AGENCY NAME & ADDRESS(if different from Controlling Office)		15. SECURITY CLASS (of this report) UNCLASSIFIED
		15a. DECLASSIFICATION/DOWNGRADING SCHEDULE

16. DISTRIBUTION STATEMENT (of this Report)

Approved for public release; distribution unlimited.

17. DISTRIBUTION STATEMENT (of the abstract entered in Block 20, if different from Report)

18. SUPPLEMENTARY NOTES

19. KEY WORDS (Continue on reverse side if necessary and identify by block number)

Earth Penetrating Weapons
Soil Material Model

20. ABSTRACT (Continue on reverse side if necessary and identify by block number)

A series of earth penetration experiments was conducted by DNA at the DRES Watching Hill Site in Alberta, Canada, in mid-July, 1974. Prior to the firings, WES had provided material property specifications for the site, and several organizations used them to calculate the event. This paper has the objective of performing a review and evaluation of the computations of penetrator performance, including consideration of zoning, material models, and other numerical models and schemes.

DD FORM 1473 1 JAN 73 EDITION OF 1 NOV 65 IS OBSOLETE

TABLE OF CONTENTS

1. INTRODUCTION

A series of earth penetration experiments was conducted by the Defense Nuclear Agency (DNA) at the Defense Research Establishment Suffield (DRES) Watching Hill Site in Alberta, Canada, in mid-July, 1974. Prior to the firings, the Waterways Experiment Station (WES) had provided material property specifications for the site, which were used by several contractors to conduct calculations of the event. This paper has the objective of performing a review and evaluation of the computations of the penetrator performance, including consideration of zoning, material models, and other numerical models and schemes.

After examining the inputs to the calculations, it was concluded that conducting detailed comparisons between the calculations themselves was not relevant. No effort had been made to coordinate the computations, and they differed widely in many important respects. As a result, there was no reason to expect that the computed stress, velocity, and strain fields should compare. The two most similar calculations were conducted by California Research and Technology (CRT) and Sandia Laboratories (SLA), both using Lagrangian codes with fairly similar zoning. However, each organization had conducted different fits to the equation of state, and the fits gave very different results. In addition, CRT had incorporated friction, whereas SLA had not. This caused the CRT computation to produce much more shearing deformation near the vehicle. CRT had used a blunted projectile, whereas SLA had used a non-blunted 9.25 CRH ogive. As a result, each material element near the axis in the CRT computation was given a much greater initial compaction than in the SLA calculation. This alone would have produced different results, even if the equation of state fits had been identical.

The incorporation of friction by CRT and its omission by SLA is the single factor which produced the greatest discrepancy between their calculated decelerations. CRT attempted to correct for their inclusion of friction by calculating the portion of the stress which was due to their friction model, and subtracting the deceleration it produced

3

from the total deceleration. It should be noted that the computations treated a highly nonlinear medium, so the notion of superposition of solutions is not valid. It is therefore inappropriate to "subtract out" one effect, such as friction, and expect to be left with a meaningful comparison. Attempting to draw comparisons of this sort can be not only inaccurate, but downright misleading. It was therefore decided to omit comparisons of calculated stress and strain fields, and to compare only the computed decelerations. To the extent possible, the measured decelerations were used as a standard of comparison for the numerical calculations.

In order to compare the computed and measured decelerations, it was first necessary to interpret the deceleration measurements. The interpretation required a knowledge of the material properties as a function of depth at the firing site itself, and a comparison of that information with the material property as a function of depth which was specified to the calculators. Section 2 is devoted to examining the rationale used to arrive at the material property specifications, and additional information which has been obtained since that specification. Section 3 interprets the deceleration data and those portions of the deceleration profile are identified which form a meaningful basis for comparison between the computed and measured decelerations.

4

2. MATERIAL PROPERTY SPECIFICATION

In studying the physical properties of the soils at the Watching Hill Blast Range at DRES, Jackson [1] concluded that the Unified Soil Classification System was too broad to adequately classify the various fine-grained sediments found in the near-surface lacustrine deposits. His work resulted in establishing an expanded system based on somewhat arbitrarily-selected criteria for liquid limit and size distribution of particles. The particle size distributions in his soil groups are shown in Figure 1a. These curves represent averages, and the actual distributions are contained within error bands about them. Liquid limit data is shown in Figure 1b.

In addition, Jackson found that each soil group displayed a characteristic variation of saturation (water content) with depth. The curves illustrating these typical saturation profiles are shown as Figure 2a. It is seen that all soil groups are fully saturated below the water table. The coarser groups, such as 5 and 6, show a rapid decrease of saturation with increasing height above the water table. On the other hand, the finer silty clays (Groups 1 and 2) stay more saturated to greater heights. This variation is attributed to the differences in capillary attraction exhibited by the various groups. Typical air void profiles are shown in Figure 2b.

At the time WES was required to establish the physical properties of soils for the EPW experiment, no data was available at the experimental site itself. Therefore, older data from nearby sites had to be used.
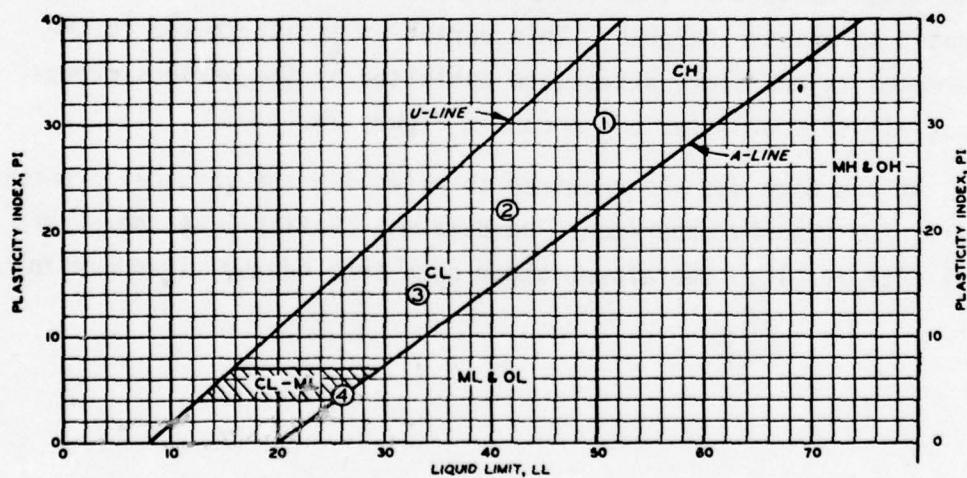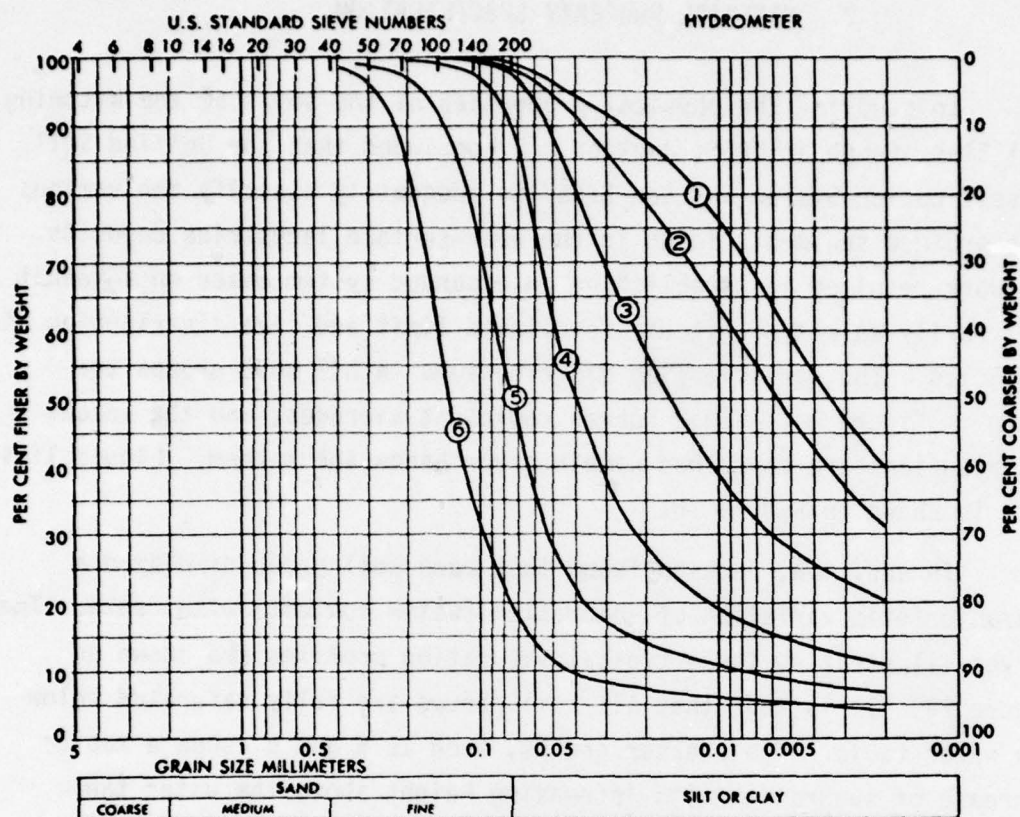
Figure 1a (top). Particle size distribution in Jackson's[1] six soil groups for Watching Hill lacustrine deposits.

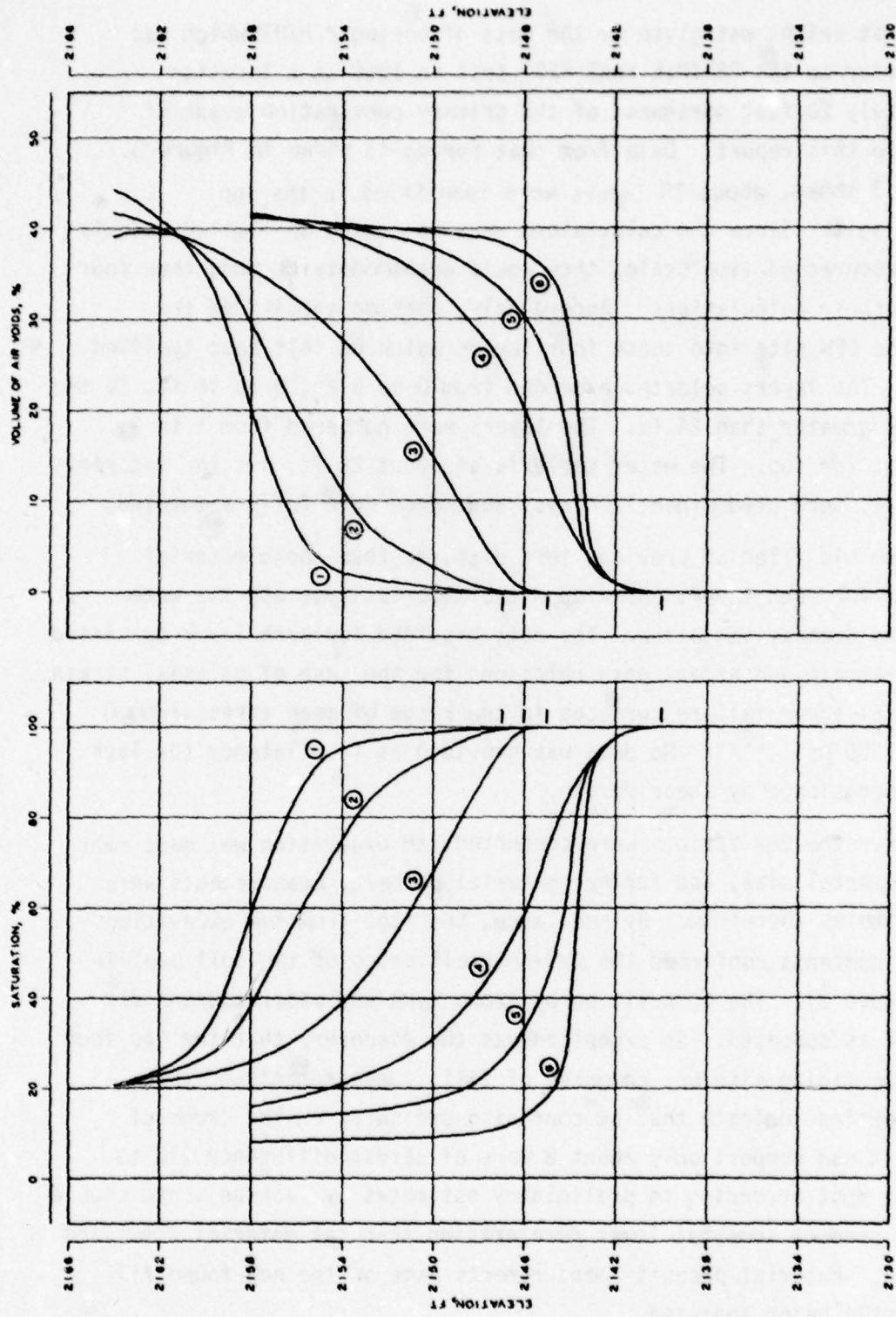Figure 1b (bottom). Typical plasticity characteristics for soil groups 1 to 4. [1]

6

Figure 2b.

Figure 2a.

Figure 2. Typical saturation and air void profiles for a portion of the Watching Hill
Blast Range, DRES. [1]

7

The greatest weight was given to the data of boring PFH/U1 which was drilled prior to the PRAIRIE FLAT HEST test in 1968 at a location approximately 20 feet northwest of the primary penetration event of interest in this report. Data from that boring is shown in Figure 3. As Figure 3 shows, about 25 layers were identified in the top 24 ft. of soil. Since the calculators were operating on limited budgets and on a compressed time scale, they could accommodate no more than four layers in their calculations. Accordingly, Jackson subdivided the soil of the EPW site into those four layers which he felt best typified the site. The layers selected extended from 0 to 8 ft, 8 to 16 ft, 16 to 24 ft, and greater than 24 ft. The layers were numbered from 1 to 4, starting at the top. The water table is at about 28 ft, but the materials below 24 ft. were predominantly clays, and hence were fully saturated.

From his files of previous test data, he then chose material properties for each layer, based upon the material type and its water content and density variation. The data provided for each layer consisted of stress-strain and stress path relations for the case of uniaxial strain, and triaxial shear failure surfaces in the range of mean stress from 0 to about 1600 psi. [2,3] No data was provided as to dilatancy (or lack thereof) occasioned by shear strain.

After the EPW firings were conducted, an excavation was made near the experimental site, and further material property measurements were made on samples therefrom. By and large, the logs from the excavation and water contents confirmed the pre-shot estimates of the soil profile (i.e., Figure 3). The composition by group type and water content are both about as supposed. An exception was the discovery that the top four feet of the firing site was composed of fill. Measurements of the fill properties indicate that at confining pressures on the order of 75 bars, it can support only about 8 bars of stress difference (10 to 15 bars at most according to preliminary estimates by Jackson), and should therefore produce somewhat lower deceleration than the material specified as layer 1. Material property measurements made on the new-found fill are currently being analyzed.
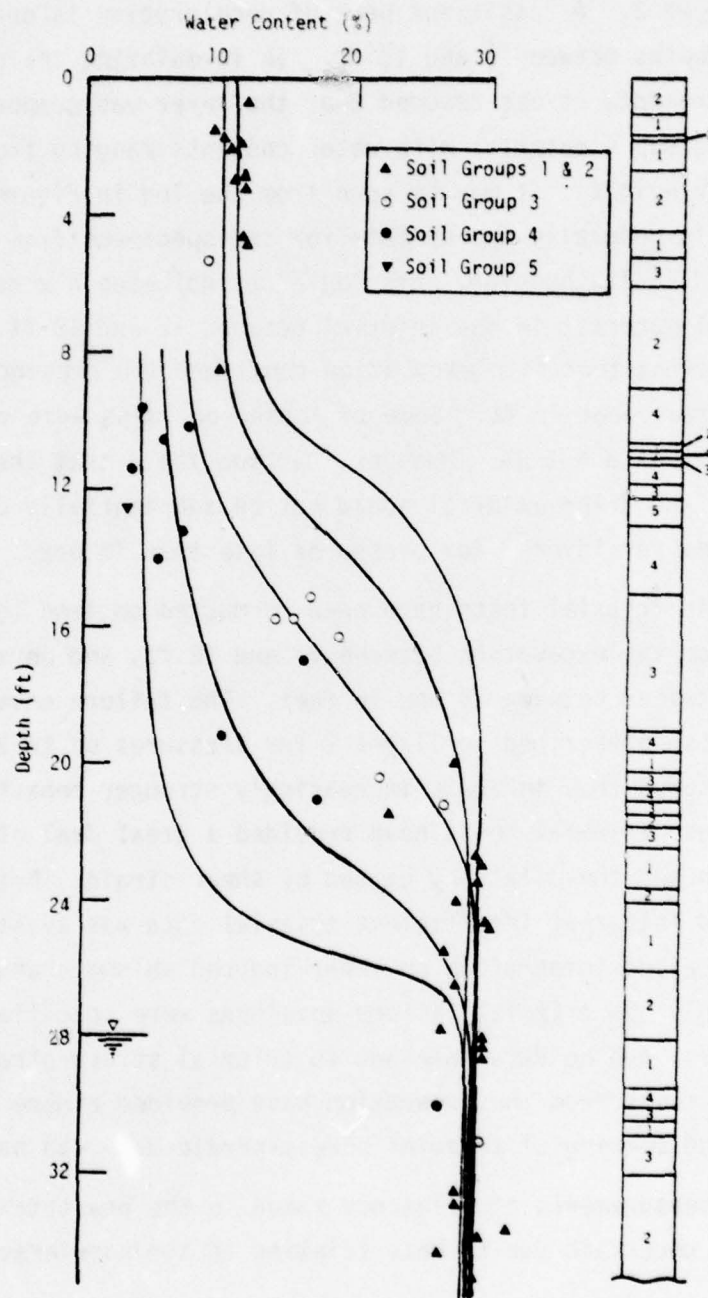
8

Figure 3. Data from boring PFH/U1, near the EPW firing site at DRES.[3]

In Section 3, comparison with the experimentally-measured projectile deceleration suggests that it might have been better to subdivide layer 2. A consistent peak of deceleration is observed in all* firings at depths between 9 and 12 ft. In formulating the properties of layer 2 preshot, it was assumed that the layer was composed predominantly of group 4 material with water contents ranging from about 4 to 10% by dry weight. It may be seen from the log in Figure 3 that this description is generally appropriate for the specimens from boring PFH/U1 between 9 and 14 ft; however, this log also indicates a zone of coarser, drier group 5 material in the interval between 12 and 13 ft. Specimens from the postshot test site excavation confirmed the presence of dry group 4 material near 12 ft. Some of those specimens were very dry, having water contents of about 3%. However, Jackson feels that the failure envelope for the drier material would not be substantially different from that specified for layer 2 for pressures less than 75 bars.

Static triaxial tests have been conducted on sand (group 5) specimens from the excavation between 11 and 12 ft, and on silt (group 4) specimens obtained between 15 and 16 feet. The failure envelopes check well with those prescribed for layer 2 for pressures up to 30 bars; at greater pressures they indicate increasingly stronger behavior. In addition, these triaxial tests have provided a great deal of information on compaction and the dilatancy caused by shear strain. Prior to the shot, WES had felt that insufficient triaxial data was available to prescribe detailed information on shear-induced volume changes (dilatancy). Therefore, only the triaxial failure envelopes were specified for the various layers, and no data relevant to triaxial stress-strain data was issued. The tests from the excavation have provided a more substantial data base, and meaningful triaxial stress-strain data can now be given.

The measurements of dilatancy taken in the new triaxial tests are somewhat uncertain due to uncertainties in the knowledge of endcap

---

*The peak in test 07 is not as pronounced as in tests 02 and 06.

friction. If the endcap friction were zero, the cylindrical samples would be expected to remain cylindrical throughout the test, and the volumetric strain would be computed as

$$\frac{\Delta v}{v_0} = \epsilon_a + 2\epsilon_r - 2\epsilon_r\epsilon_a + \epsilon_r^2 (\epsilon_a - 1) \tag{1}$$

However, if the endcap friction is so high as to permit no slippage, then there is no radial strain at the endcap, but a large radial strain near the center of the specimen where the strain is measured, and volumetric strain would then be computed as

$$\frac{\Delta v}{v_0} = \epsilon_a + \epsilon_r - \epsilon_r\epsilon_a + \frac{\epsilon_r^2}{3} (\epsilon_a - 1) \tag{2}$$

Jackson feels that the endcap effect can cause an error as great as a factor of two in the computed volumetric strain. In either case, the test results should provide important new data to contribute to the understanding of the material properties.

11

3. THE DRES EXPERIMENTAL DATA

This section addresses the question of how meaningful it is to compare the computed decelerations with those measured in the DRES test. If the comparison is to have meaning in a given depth interval, the material properties must be well specified, and the decelerations must be accurately measured. Strictly from examining the deceleration data and using consistency arguments, it is possible to identify depth intervals where both of these requirements are not met. Using this and other information, it is concluded that there are only two limited depth intervals in which it is potentially meaningful to draw the comparison. These are:

1. The depth interval between 16 feet and 24 feet where the actual measurement is constant at 39 g's to within 21%, and

2. The depth interval between 4 feet and 8 feet, where the actual data oscillates between 42 and 95 g's, but which might be interpreted as a constant deceleration of 75 g's modified by a spurious oscillation.

The other depth intervals exhibit wide ranges of deceleration which we believe are real. As a result, they cannot be adequately described by a single equation of state. The failure to discriminate among the soil types which produced very different decelerations reflects the state of the art of penetration prediction at the time the material property fits were conducted.

The material property data supplied to the calculators assumed that the soil was disposed in four uniform layers, each of the top three being eight feet thick, and the bottom layer extending as deep as necessary. As it turned out, this assumption by itself dictated the form of the computed deceleration profile in the upper three layers. The penetrator parameters were such that a nearly-constant deceleration is produced in a given uniform eight foot layer. All of the calculations reflected this fact. They differed only in the magnitude of the deceleration calculated for each layer.

12

As a consequence, the calculations can agree well with the data only if the data is reasonably constant in each eight foot layer. If the data does not have that form, we must conclude either that there is a variation of material properties in the layer such as to produce a range of very different decelerations, or that there were errors in the deceleration measurements. This consistency argument provides a screening test which weeds out bad intervals, and identifies potentially good intervals.

The deceleration data is shown in Figure 4. At face value, it is reasonably constant only in one of the layers; namely, layer 3, between 16 feet and 24 feet, where it has an average value of 39 g's with oscillation between 31 and 46 g's. However, closer scrutiny shows that there is apparently a spurious 150 Hz oscillation superimposed on the real data. The oscillation apparently has a very large amplitude (plus or minus 20 or 30 g's) at early-times, but damps down to plus or minus a few g's at the end of the penetration. This behavior is suggestive of a penetrator structural vibration mode which is excited in the acceleration phase, or on impact. However, such a mode has not been identified, and the source of the oscillations is at present not understood. In an effort to extract more information from the data, we have postulated an idealized deceleration profile in which these oscillations are smoothed out. The philosophy adopted was to select regions conforming as well as possible to the eight foot layers, and to select a constant deceleration in each region which would produce about the same velocity decrement as the integrated measured curve.

This philosophy biases the result in favor of identifying regions which are consistent in the sense discussed above, and which could be potentially useful to compare with the calculations. The resulting idealized profile is shown in Figure 4. The figure also shows a smoothed profile constructed independently by Hadala.[4]

The two smoothed data sets have several features in common:

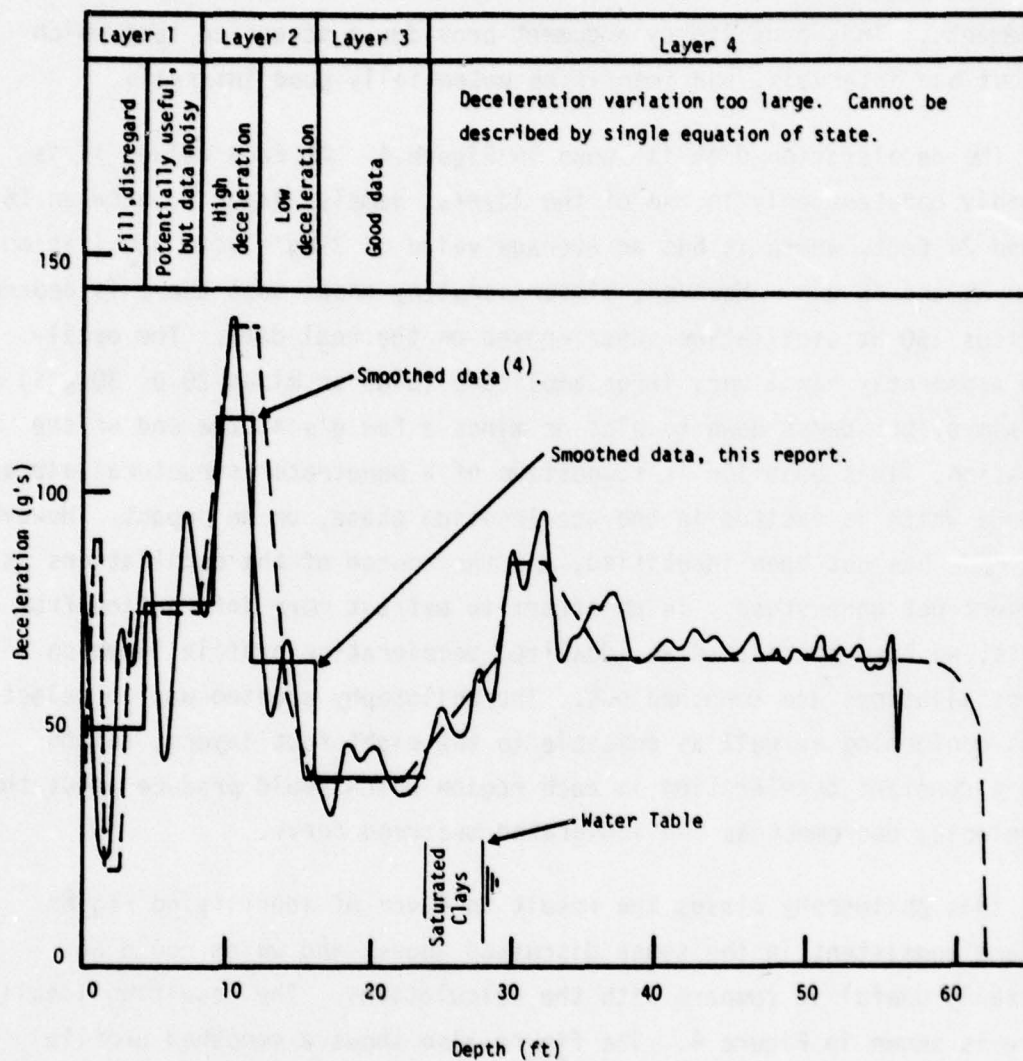1. A region of constant deceleration in the depth interval from

13

Figure 4. Measured decelerations for shot 6 of 7/15/74. Step curve
is hypothesized idealization, conforming to the soil layers
shown.

4 to 8 feet. This is the lower portion of WES layer 1. This suggests that apart from the top four feet of fill, a uniform deceleration of about 75 g's is provided by the material of layer 1. Unfortunately, the data exhibits a particularly large oscillation loop in this depth interval, ranging from 95 to 42 g's. Although it is possible to interpret this data as a constant deceleration of 75 g's modulated by a spurious oscillation, other interpretations are certainly possible, and a large measure of uncertainty remains.

2. A region of high deceleration in the interval from 10 to 12 feet, with lower deceleration regions adjoining it. This suggests that there is a great deal of variation in the material properties in WES layer 2. The different properties produce a range of decelerations between from 115 to 130 g's maximum to a minimum of from 40 to 63 g's.

3. A region of constant deceleration in the depth interval from 16 to 24 feet. Both smoothed fits indicate a deceleration of about 39 or 40 g's in this interval.

4. While we did not attempt to smooth the data below 24 feet, both the data and Hadala's fit indicate that the deceleration varies between 40 and 85 g's in this region.

The smoothed curves strongly suggest that the region between 8 and 16 feet, which WES characterized as layer 2, should be subdivided into two layers to reflect the high and low decelerations measured there. The other firings at the DRES site confirm the peak in the deceleration curve at a depth of about 12 feet although it is less pronounced in firing 07. Figure 5, taken from Reference 4, summarizes the deceleration records for firings. The impact velocity and penetrator data for those firings are given in the legend. The deceleration was measured by accelerometers which were carried on board the penetrator. The data were read out in two ways. First, the data were transmitted out in real time during the penetration process. Second, the data were recorded in an onboard memory unit during penetration, and were telemetered out after the penetrator came to rest.

15

TABLE 1

| Depth Interval (ft) | Idealized Deceleration (g's) | Material | Calculated Deceleration (g's) | | |
| | | | CRT | | |
			Friction	Total	SLA
0-4	49	Fill	--	--	--
4-9	75	Layer 1	53-65	100	55
9-12	115	Layer 2	80-87	125	55
12-16	63	Moister, finer grained than Layer 2	--	--	--
16-24	39	Layer 3	20	47	35
> 24	Varies	Varies	--	--	20*

*First 0.4 meters.

Table 1 summarizes the measured decelerations as given by our smoothed treatment, and compares them with the calculations of CRT and SLA. The calculations are discussed in Section 4.
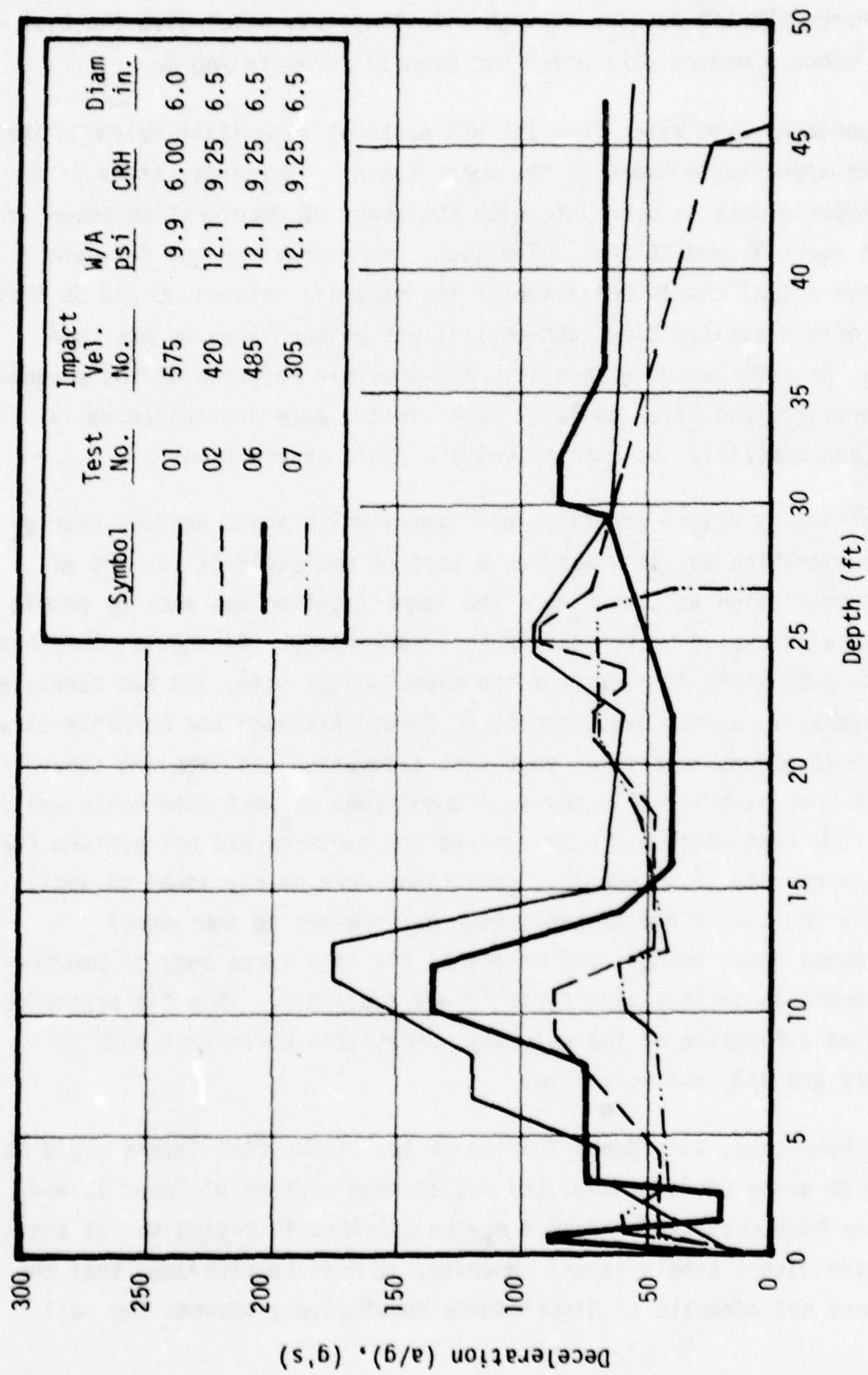
Figure 5. Measured decelerations for firings at DRES, showing consistent deceleration peak near 12-ft depth.

17

Figure 5 represents the data by straight-line segments which give the best
fit to the onboard memory data which has been filtered to 200 Hz.

No specimens were taken from the WES postshot excavation below 25 feet
which is the approximate depth of the water table. Therefore, there is no
material property data to correlate with the peaks of deceleration shown in
Figure 4 at about 31 and 36 feet. The logs from nearby borings indicate
only that the visual characterization of the material between 30 and 35 feet
is that of gray saturated clay, and that it was either sandy or has thin
sand strata, or sand lenses within it. The possible relation of the predom-
inantly coarse-grained layer to local peaks in the deceleration curve is
supported (but certainly not conclusively) by this observation.

The effort by WES to identify soil layers which would produce nearly-
constant deceleration may be viewed as a test of the state of the art of
penetration prediction at that time. The identification was made by people
who had a very extensive background in soil technology. As inputs, they had
samples from a borehole 20 feet from the experimental site, and had conducted
numerous material property measurements on them. Although the borehole data
was a few years old at test time, post-shot excavation and sampling showed
that for the most part it reflected soil conditions at test time quite well.
(The upper four feet which had been removed and replaced did not perturb the
results substantially.) In summary, conditions were nearly ideal to apply
the then-existing technology of penetrator performance to the identi-
fication. Among other things, the empirical fit to a large body of penetra-
tion experiments in various soil types[5] was available. This fit prescribes
penetration as a function of the velocity, penetrator parameters such as
nose geometry and W/A, and soil type.

As we have seen, the identification of two of the four layers could be
interpreted as quite good; namely, the undisturbed portion of layer 1, and
layer 3. The poor results in layer 4 may be ascribed to trying to fit too
large a region with a single layer. However, it must be concluded that the
technology was not adequate to discriminate conclusively between the soil

18

types in layer 2 which produced a deceleration of 115 to 130 g's, and those which produced between 40 and 63 g's.

4. COMPARISON OF CALCULATIONS AND MEASUREMENTS

4.1 THE CALCULATIONS

Five "hydro" code calculations of the EPW deceleration have been conducted in connection with this program [6,7,8]. The greatest weight will be given to the calculations of CRT, and to the SLA rigid body computations. These computations are singled out because their zoning was most nearly adequate, and because the computing programs were properly selected to give adequate results.

The best way to determine whether the zoning is adequate is to conduct a sequence of computations using successively finer zones. When the zone size becomes fine enough to resolve the important physical features of the problem, the calculations converge in the sense that finer zoning does not influence the solution. Even in such a study, judgment must always be exercised to assure that all important physical features have been resolved.

At the time of this writing, SLA had conducted a limited zoning study using square zones having sides of 6, 3, and 1.5 centimeters. Only layer 1 material was considered, without friction, and an ogival rigid body with non-blunted tip was used. The results indicated that the computed deceleration increased somewhat when the zone size was reduced from 3 to 1.5 centimeters. The stresses computed along the projectile varied significantly, but the greatest variation was near the nose tip, where the stresses act only on a small area to produce the projectile deceleration. Thus the deceleration appears to be computed reasonably well, but finer zoning might be necessary to accurately compute the stresses produced on the surface of the vehicle. This information would be required, for example, in a study to analyze the structural response of the vehicle.

20

CRT has conducted a zoning study which will be discussed later in this section. However, the computations were not carried out to sufficiently late times to provide a meaningful result. Also, it is not appropriate to judge the zoning of the CRT calculations on the basis of the SLA study. The CRT computations included the effects of a large friction coefficient, which produced much more shearing strain in a narrow region near the projectile surface, and might therefore require much finer zoning than the SLA calculations.

Both the CRT and SLA rigid body computations show that the largest stresses are produced near the vehicle nose, and they decrease rapidly with distance along the projectile, falling to very low values at the "shoulder" of the ogive. Thus, several zones are needed along the length of the projectile nose (49.5 centimeters) to resolve the stress field and predict the deceleration. In addition, the stress falls rapidly with radial distance. At the point where the stress is greatest (near the tip), the SLA calculations shows that it falls to 10% of its peak value in a radial distance interval of about 10 centimeters. The PI calculation [8] was too crudely zoned to resolve these stresses. The first few zone boundaries in the radial direction were initially at radii of 7.7, 17, 28, 41.4 and 57.3 centimeters. This may be compared with the penetrator radius of 8.255 centimeters. The initial zone length in the axial direction was 24 cm, providing only about two zones along the length of the ogival nose. It would thus be meaningless to compare the stress fields computed by PI with those of CRT and SLA. Moreover, the computed deceleration must also be suspect. Accordingly, we shall not discuss the PI calculation further in this paper.

SLA conducted a computation using CSQ, an Eulerian code. However, CSQ did not contain several state of the art computing features, which undoubtedly contributed to the poor quality of the solution obtained. One major deficiency was the manner in which the projectile-soil boundary was treated. The boundary was defined only by the array of "mixed" cells which were intersected by the projectile boundary. The boundary is thus described as a histogram. In the mixed cells, all

21

thermodynamic and hydrodynamic properties were taken to be some average of the constituent materials, which in this case are steel and soil. Because these two materials have radically different properties, great inaccuracies are produced in the stress computed in a mixed cell.

A second source of inaccuracy was the nature of the equation of state used in the CSQ calculations. In particular, CSQ did not use an adequate model of the crush curve, but assumed that porous materials have zero mean stress until they are compressed to the poreless solid density.

In fairness, it should be noted that SLA recognized the shortcomings of CSQ in advance, and devoted only a modest effort toward this computation.

There are other Eulerian codes in existence which have the ability to define the projectile-soil interface by a string of tracer particles. This provides a means to define the volumes in the mixed cells which are occupied by the two material species, so that the stress can be more accurately calculated in them. It also permits the computation of those areas across which transport may occur at the cell interfaces. These codes can also treat more sophisticated material models than CSQ. In short, there are many other Eulerian codes which could treat the problem much more accurately.

However, all Eulerian codes with which the author is familiar have inherent shortcomings for problems of this type. Among these are the tendency of Eulerian codes to diffuse physical properties when the material moves through the computing grid. Since the equations of state (constitutive relations) used in these computations are path dependent, one must keep track of the stress-strain history which each material element has experienced. If the cap model is used, for example, the parameters specifying the current geometry of the cap must be known for each material element. In other cases, the peak volumetric compression which each element has experienced must be known. This information tends to diffuse from a given material element to its neighbors as transport through the computing grid occurs. A second shortcoming is the lack of a good algorithm to compute and apply the deviatoric stresses in cut cells. Thirdly, the presence of small cut cells leads to stability problems, and often requires inordinately small time steps to avoid large oscillations.

22

Eulerian codes have been successfully applied to many penetration problems where these shortcomings have not led to unbearable inaccuracies. The use of CSQ has not provided an adequate test of the ability of an Eulerian code to compute the EPW problem.

The SLA deforming body calculation used 3 centimeter zones in the soil, and for the reasons discussed below, probably gave the best prescription of the vehicle's overall deceleration. However, large oscillations in both stress and particle velocity were computed within the vehicle. The oscillations rendered the velocity and stress contours within the vehicle incomprenensible, so that these quantities are not available for analysis.

Near the penetrator, CRT used zones which were 4.13 cm in height and width, which provided more than 10 times as many zones near the penetrator than did PI. The SLA calculation to be discussed here used zones which were 3 cm. in both height and width, which provides even better resolution. CRT and SLA both used Lagrangian codes in these calculations. [6,7]

The constitutive relations used in the CRT and SLA rigid body calculations differed appreciably. Frictional forces on the projectile's surface were employed in the CRT computation, but not in SLA's. The CRT computation employed the failure locus defined by triaxial compression test data as the yield locus in an elastic-ideally plastic model. A non-associative flow rule was used which results in no volumetric plastic strain. SLA, on the other hand, chose to fit the data by means of a cap model together with an associated flow rule. This model produces volumetric plastic compaction immediately upon the application of any strain which produces a compressive mean stress. The specification of the cap geometry and its variation with volumetric plastic strain had to be very arbitrary, since no data on dilatancy was provided to the calculators by WES. The approach taken by SLA was to utilize the same equations as in a previously-coded model and to prescribe the parameters of that model in such a way as to reproduce the data provided. This attempt was only partially successful in that the paths produced in the τ-p* plane did not show good agreement with the uniaxial strain data

---

* The deviatoric stress, τ, and the mean stress, p, are precisely defined in Appendix A

provided by WES. The path in τ-p space which the material followed in the penetration calculation was not close to that in uniaxial strain, but was concave upward in the τ-p plane and intersected the triaxial failure locus at about the point where the cap and failure locus inter- sect. Upon unloading the path retraces the triaxial failure locus, for the points which SLA has monitored.

Qualitatively similar comments can be made relative to stress paths in the CRT calculations. They also traverse paths which are concave upward in the τ-p plane, until they attain the yield locus, and then subsequently unload upon that locus. Since both equation of state models contained accurate fits to the failure locus, one might suppose that this leads to essentially the same material properties specification. However, one must recall that the SLA model produces plastic compaction on loading, and plastic dilatancy when moving along the failure locus. CRT's model provides no dilatancy anywhere. Therefore, different results are to be expected from this source. Since there was no material property data to guide SLA's specification of volumetric plastic strain, it had to be completely arbitrary. Therefore, its incorporation into the computation adds little to the computations' credibility. The SLA cap model is discussed in detail in the Appendix.

In each of the rigid body calculations, it was assumed that the stress which decelerated the projectile was that in the center of the soil cell adjacent to the projectile. This assumption produces a numerical error which decreases as the cell size decreases. In actuality, the stress on the projectile must exceed the stress in the adjacent cells if the projectile is to cause an acceleration of those cells. Therefore, under the conditions of the experiment under discussion, this assumption always leads to underestimating the projectile's deceleration. The underestimate is purely a feature of the numerics employed.

There are two separate indications which substantiate these remarks. These are:

• The increased deceleration which results when the fineness of the computing zone is increased.

24

● The increase in deceleration computed when a deforming body
   is used in computation.

In the case of the Sandia computations, the deforming body
computation gave peak deceleration of 75 g's, compared with 55 g's for
their rigid body computation. [7] This difference arose despite the
fact that the same zone size was used in the soil in both computations.
Peak pressures of 14.5 MPa were produced in the deforming body case
compared with 8.5 MPa in the rigid body case. Unfortunately, SLA used
a blunted tip in their deforming body calculation, and an unblunted
ogive in their rigid body computation, which makes the comparison less
direct.

Since the deforming body deformed by no more than 30 microns
radially anywhere, the deformation itself did not change the deceleration
noticeably. In a deforming body computation, the stress in the body is
actually calculated, and is used to accelerate the surrounding soil.
In accordance with Newton's third law, it also decelerated the penetrator.
The higher computed deceleration of the deforming body is therefore
proof that higher stresses are computed on that body than in the rigid
body calculation.

CRT has conducted zoning studies using blunt-nosed rigid pene-
trators and the soil of layer 1.[10] The velocity used was 1500 ft/sec.
Those studies suggest (but not conclusively) that higher decelerations
are produced as the mesh size decreased. The calculations are summarized
in Figure 6.

Although suggestive, the zoning studies of CRT were not definitive,
because they encompassed time spans of only 0.2 to 0.3 msec during which
the vehicle moved only about 3 to 5 inches, despite its initial velocity
of 1500 ft/sec. In addition, the computations were initiated with the
nose partially buried. Therefore, the results are somewhat obscured by
the initial "slap" which the projectile experiences at early times when
the partially buried nose interacts with a substantial volume of soil
which is at rest. Because of this effect, the finely-zoned cases exhibit
high initial decelerations, which then slowly decrease with time, e.g.,

25
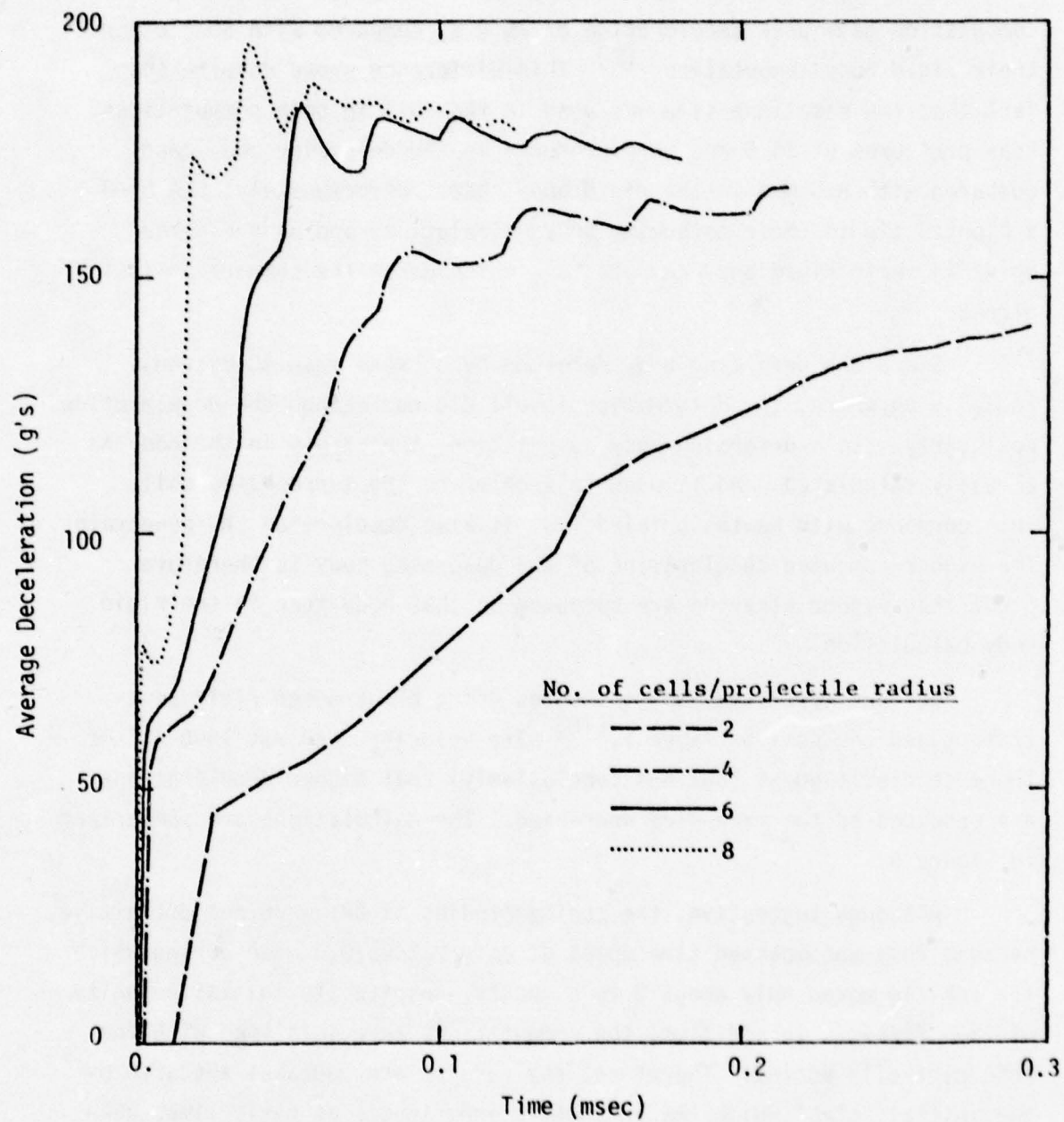
Figure 6. CRT study of dependence of computed deceleration on zone size, at 1500 ft./sec. into layer 1 material.

6 and 8 zones across the penetrator. The more coarsely-zoned cases show increasing deceleration throughout the whole 0.3 millisecond interval. (The CRT calculation discussed earlier in the paper had 2 zones across the penetrator.) Throughout the time intervals shown in Fig. 6, the finer-zoned cases all show higher decelerations than the coarser-zoned cases. However, all the curves are converging, and one cannot rule out the possibility that they might all come together at some later time. On the other hand, there is certainly not enough data to conclude that they will definitely come together at later times. To obtain a definite conclusion, the calculation should be run several times farther (in time).

An additional uncertainty is introduced by the fact that in the few inches of penetration considered, the flow pattern which characterizes the penetration after nose embedment never arises. In particular, flow around the "shoulder" of the ogive is not attained. This phenomenon could also be investigated if the computations were carried further.

4.2 COMPARISON WITH THE IDEALIZED DECELERATION PROFILE

The decelerations as a function of depth computed by CRT and SLA using their rigid body models are presented in Figures 7 and 8. For the reasons discussed in Section 4.1, the computed decelerations are probably too low. This will not be repeated in the following text, but should be borne in mind by the reader.

4.2.1 Layer 2

As we have discussed, the postshot excavation, and subsequent tests by WES suggest that the material near 12 ft was that whose properties were specified by WES as layer 2. Therefore, it is of interest to compare the decelerations computed by SLA and CRT for layer 2 with the experimentally measured deceleration of about 115 g's. We may note that CRT, who included friction in their model, computed about 125 g's. SLA, who did not include friction computed only 55 g's. A possible conclusion is that the amount of friction used by CRT is close to the proper one for this material, and that dilatancy is unimportant.

However, the triaxial tests conducted by WES on the materials of Group 4 consistently show a large amount of dilatancy. The dilatancy commences almost immediately upon application of deviatoric stress, and is large enough so that the volume of the specimen increases even though the mean stress attains substantial levels. Therefore, the possibility exists that strong dilatant effects, rather than friction, is responsible for the high deceleration. In this connection, one may note that the SLA model included the effects of dilatancy, whereas that of CRT did not.

From the data we have, it is not possible to decide how much dilatancy the model of SLA provided along the stress-strain paths which were followed in their computation. It would seem fruitful to ascertain this, and to compare it with the dilatancy measured by WES, which is due to be published soon. If the SLA model and WES experiments indicate the same amount of

Phase I Calculation

Constant deceleration (125 g) in Layer 2

Phase II Calculation (Nose entering Layer 3)

Axial force and deceleration due to friction

Constant deceleration (47 g) in Layer 3

Axial Force on Penetrator -- 10^3 lb
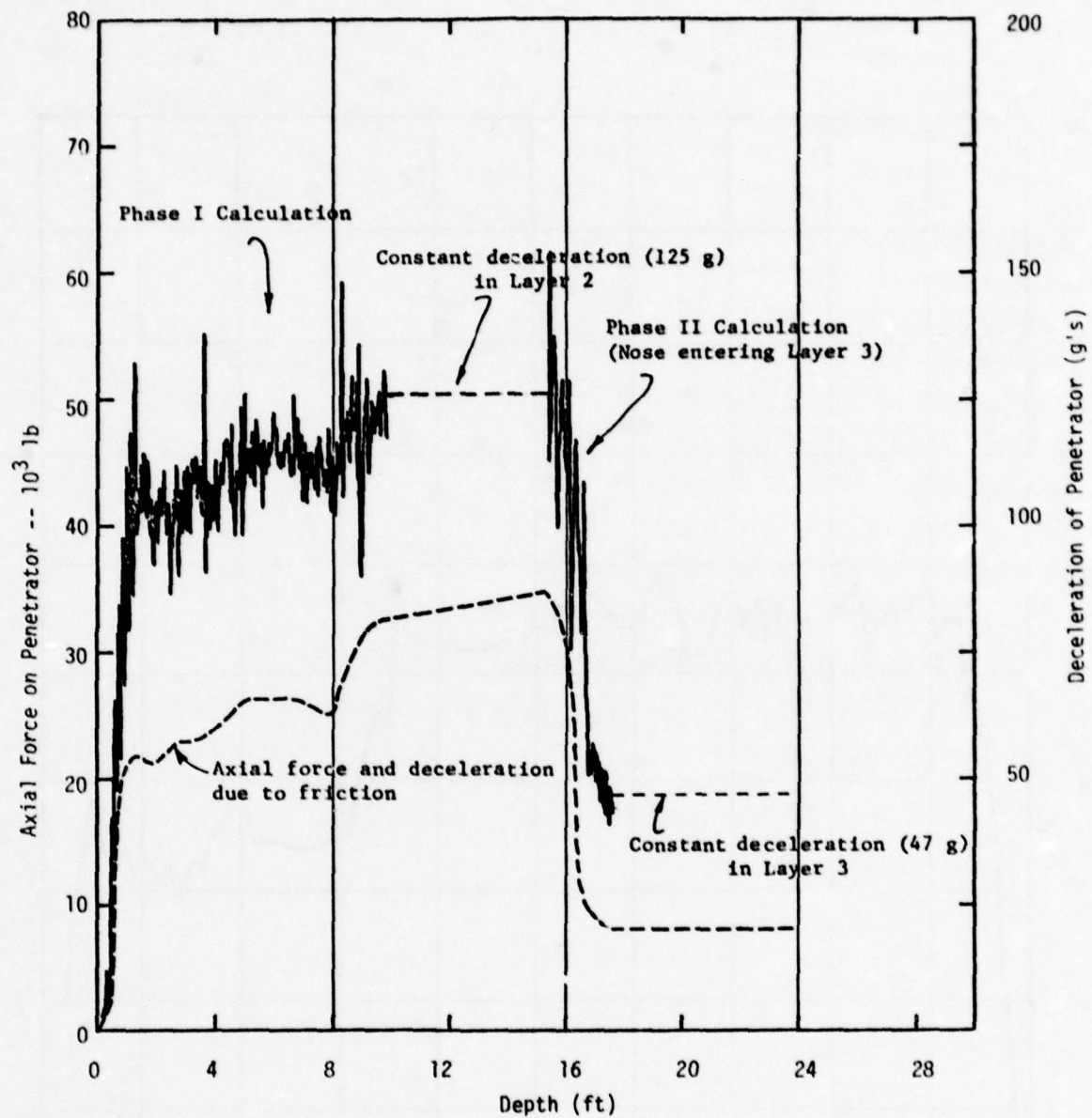
Deceleration of Penetrator (g's)

Depth (ft)

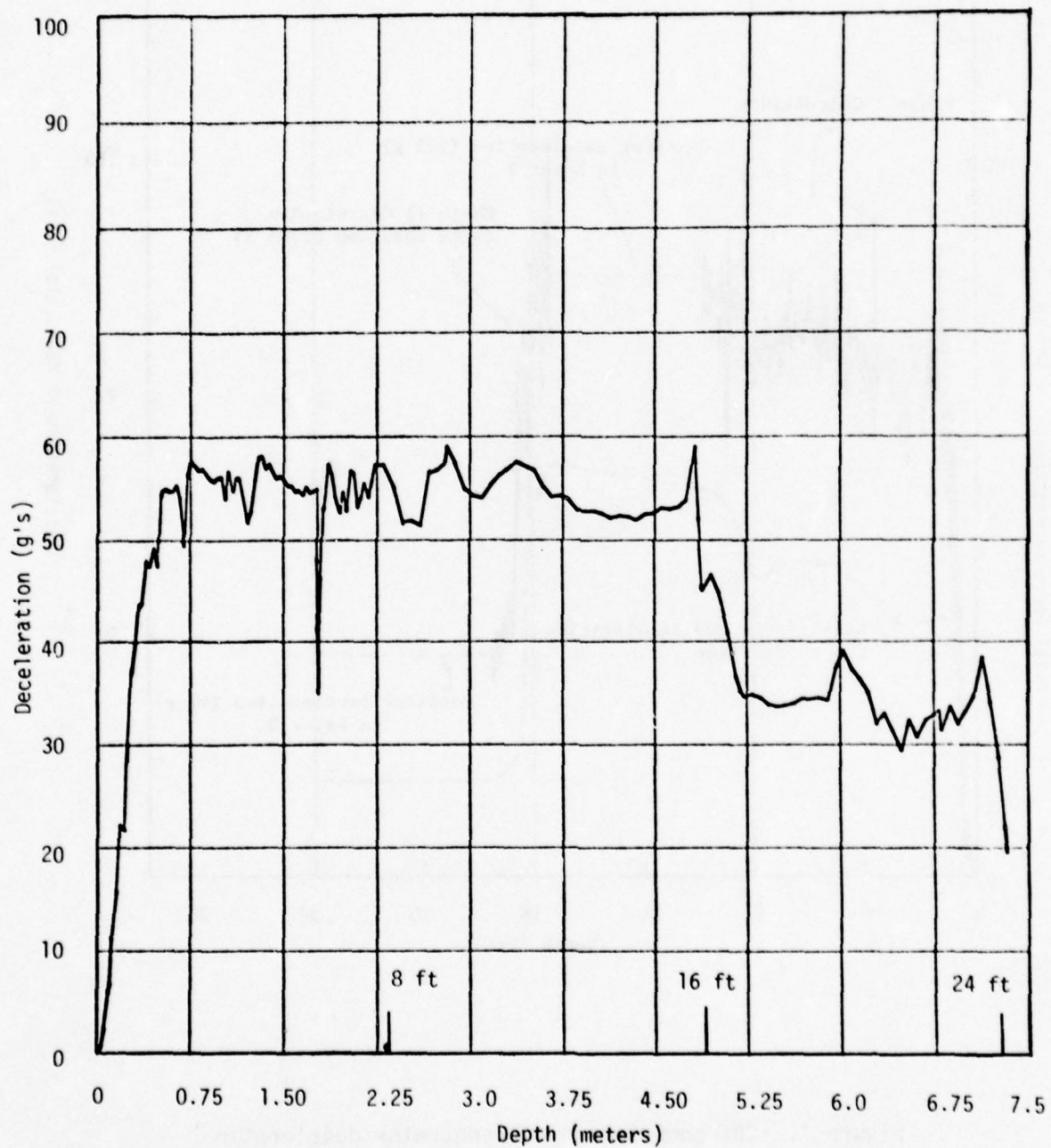Figure 7. CRT computation of penetrator deceleration.

Figure 8. SLA computation of penetrator deceleration.

dilatancy, then one can discount dilatancy as the factor which causes high deceleration. If it does not, then a material model should be constructed having the appropriate amount of dilatancy and used in a computation to see whether it produces the measured deceleration.

The materials in layers 1 and 3 exhibit much smaller dilatancy than that in layer 2, so that the above remarks on dilatancy do not deserve as much emphasis for them. However, it seems worthwhile to at least check the relevance of dilatancy for these layers when the new triaxial data of WES become available.

4.2.2 Layer 1

Figure 7 shows that CRT computed an average deceleration of about 110 g's in layer 1, of which 53 to 65 g's arise from their friction model. As shown in Figure 8, SLA computes 55 g's, which is in rough agreement with the CRT computation with the friction subtracted out. The computations may be compared with the 75 g's of the idealized deceleration profile of Figure 4. Note that the SLA deforming body calculation gave 75 g's. These results show that using the WES data in these codes gives reasonable agreement with the measured decelerations without adding friction.

4.2.3 Layer 3

Figures 7 and 8 show that CRT and SLA computed 47 and 35 g's, respectively in layer 3, with friction contributing about 20 g's to the CRT calculation. These may be compared with the 39 g's of the idealized deceleration profile of Figure 4. Again, the results suggest that a well-zoned computation using only the WES data would give suitable agreement with the measurements without adding friction.

4.2.4 Layer 4

CRT did not conduct computations in layer 4. SLA computed until the penetrator nose was 0.4 meters (1.3 ft) into that layer, obtaining a deceleration of 20 g's. Their calculation was terminated at that point

since they felt that the material model for layer 4 was responsible for the very low deceleration.

A wide range of decelerations was measured. Figure 4 indicates a peak deceleration of 95 g's, with a typical deceleration at late times of about 70 g's. The reason for the substantial difference between computed and measured decelerations is presently unknown. Since it is important to understand the decelerations produced by saturated materials beneath the water table, an effort should be made to resolve this discrepancy.

5. RECOMMENDATIONS AND CONCLUSIONS

The different soil layers of the DRES site produced very different decelerations of the EPW. The range in decelerations, as deduced from the idealized deceleration profiles, is from about 115 g's in layer 2 to 39 g's in layer 3. The velocities corresponding to these two extreme decelerations is 450 and 400 f/s, respectively.

Table 1, on page 14, summarizes the best estimate of the experimentally measured deceleration as a function of depth, and the computed results of CRT and SLA in the various WES layers. As discussed in Section 3, it is only meaningful to compare the measured and computed decelerations in the depth intervals of 4 to 8, and 16 to 24 feet. In the interval 4 to 8 feet, CRT computed a deceleration of 100 g's, while SLA computed 55 g's. The experiments suggest an average of 75 g's for this interval, with oscillations between 42 and 95 g's. In the interval between 16 and 24 feet CRT computed a deceleration of 47 g's, while SLA computed 35 g's. The measured value is 39 g's $\pm$ 21 percent. Evaluation of the computations indicates that a properly zoned calculation with an improved algorithm for computing surface stresses on the EPW could reproduce the measured decelerations without using friction.

It is concluded that the computations discussed herein predicted too low a deceleration because of the numerical procedures and zoning used. Either the deforming body should be used in the computations, or an algorithm should be formulated which provides a better prescription of the stress on the surface of the rigid body model of the penetrator. The SLA computations indicate that the present algorithms produce an error of about a factor of $75/55 = 1.36$ for layer 1 material. It is felt that the new algorithm will probably reduce the zone fineness required to compute the correct deceleration. Being able to use the rigid body model will be much more economical than using a deforming body.

Zoning studies should be conducted for a substantially longer time than 0.3 milliseconds to determine the zone size required for an accurate computation of the deceleration for the model used by CRT.

33

The data on dilatancy being generated by WES for layer 2 material should be incorporated into a computer code material model and runs made to see whether dilatancy is responsible for the high observed decelerations. This effort should result in deciding what combination of friction and dilatancy is needed to predict deceleration in dry Group 4 materials. If the hypotheses of this paper prove to be valid, then friction and dilatancy are of secondary importance in layers 1 and 3.

No satisfactory computation has been conducted in layer 4. The measured decelerations are not in accord with the material properties specified by WES. Therefore, this region deserves more attention, both with respect to material property determinations and computations.

New material models should be prescribed for the two regions of layer 2. The layer of fill comprising the top four feet should be taken into account.

The material property data derived from laboratory tests was insufficient to completely specify the material model. Soil elements in the computations followed different load-unload paths than were used in the measurements. As a result, it was necessary for the calculators to make arbitrary assumptions as to how the material would behave along the new paths.

SLA chose to assume that the material obeyed a particular cap model with an associated flow rule. Now cap models have the important attributes of insuring uniqueness and continuity (except for some specific instances which will be discussed in what follows). While these are worthy attributes, the cap model is not the only way to accomplish these objectives. There is no argument which suggests that soils must obey either a cap model or follow the associated flow rule. Indeed, laboratory measurements have shown cases where soils do not obey the associated flow rule. We shall also discuss aspects of the SLA cap model which are physically unrealistic. It prescribes a behavior which no material could possibly follow. Another point which

34

should be stressed, is that geometric details of the cap model, which users tend to vary almost casually, exert profound and far reaching influences on the material behavior.

In summary, choosing to use a cap model represents a far-ranging hierarchy of assumptions, which are embodied in the detailed geometry of the failure locus and cap, as well as in the specific parameters used in the model. CRT chose also to incorporate friction, which exerted a much larger influence than the details of the material model. The friction served to create a larger shearing (deviatoric) strain than appeared in the SLA calculation. Because CRT used a non-associated flow rule, the increased shearing strain did not lead to increased dilatation. If friction were included in the SLA model the resulting larger shear strain would produce much more dilatation. Thus, there would be a much stronger coupling between friction and other aspects of the material model in the SLA case.

These arguments make it more plausible for CRT to attempt to correct for their use of friction by subtracting out the stresses due to their friction terms, but by no means justify the correction. The only conclusion is that completely different material models were used in the two cal- culations, and there is not enough good experimental data to discriminate which is more nearly correct. The only conclusion which can be drawn is that there is not a friction effect of the magnitude postulated by CRT, except possibly in a limited depth region near 12 feet.

In this regard, it would have been beneficial to have CRT repeat its calculation without friction. The single argument against doing so was the cost associated with conducting the additional computation. This provides another example of the impact of economic considerations on a scientific research program. If the cost of computations of this sort could be reduced by an order of magnitude it would do away with restric- tions of this sort which prevent the resolution of an important question.

A question which naturally follows is, "How does one decide what material model to use?" The answer cannot in general come from purely theoretical considerations. One must resort to some experimental verification to justify the use of the model. The most direct detailed justification comes from material property measurements along the important load-unload paths. In the absence of such data, one can obtain a less direct and more ambiguous justification by comparing the results of some other experiment, such as the deceleration versus time of the EPW. Unfortunately, this comparison can be very ambiguous in this case, as there are undoubtedly many different material models which would produce about the same result. However, it is the only means at our disposal at this time.

Examination of the calculations revealed that many material elements followed the same type of load-unload paths. The typical paths are illustrated in the sketch. Loading generally fell beneath the failure locus, and unloading quickly attained the failure locus and then proceeded along it. Thus, the details of the unloading along the failure locus were important to the calculational results.
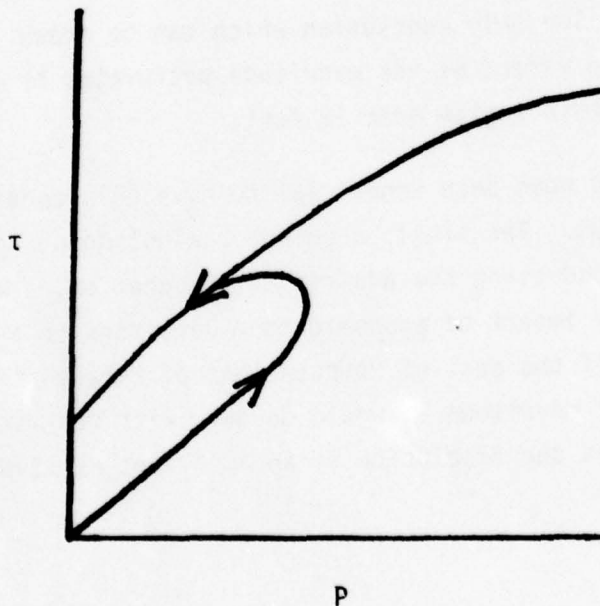
Because unloading along the failure locus is an important aspect
of the calculations, the suggestion was made by the author that WES conduct
unloading tests along the failure locus. Such a test would reveal how the
material actually behaves in such a process, including how much dilation
occurs. It would also indicate whether or not this material follows an
associated flow rule in the process. It was felt that such a test is
presently beyond their capabilities. However, discussions indicated
how their capabilities could be augmented to accomplish the test, and
it is recommended here that this be done.

REFERENCES

1. Jackson, J.G., Jr., "Physical Property and Dynamic Compressibility Analysis of the Watching Hill Blast Range", U.S. Army Engineer Waterways Experiment Station Technical Report S-72-4, April 1972.

2. Jackson, J.G., Jr., "Recommended Soil Profile and Properties for DNA Penetrator Test Site, DRES, Canada", Memorandum dated 29 March 1974, U.S. Waterways Experiment Station.

3. Jackson, J.G., Jr., "Soil Classification and Triaxial Shear Test Data for DNA Penetrator Test Site, DRES, Canada", Memorandum dated 30 May 1974, U.S. Waterways Experiment Station.

4. Hadala, P.F., "Evaluation of Empirical and Analytical Procedures Used for Predicting the Rigid Body Motion of an Earth Penetrator", U.S. Army Engineer Waterways Experiment Station, Miscellaneous Paper S-75-15, June, 1975.

5. Young, D. Wayne, "Depth Prediction for Earth-Penetrating Projectiles", Journal of the Soil Mechanics and Foundations Division, ASCE, Vol. 95, No. SM3, Proc. Paper 6558, May 1969.

6. Wagner, M.H., et al., "Numerical Analysis of DNA Earth Penetrator Experiment at DRES", California Research & Technology, Inc., CRT 2050-2, October 1974.

7. Byers, R.K., et al., "Predictions of Projectile Penetration Phenomena and Comparison with Experiments in a Soil Medium", SAND 75-0174, April 1975.

8. Orphal, D.L., et al., "A Computation of a DNA Earth Penetration Experiment at the Watching Hill Site, DRES, Canada", Physics International Report PIFR-678, December 1974.

9. Patterson, W.J., "DNA/Sandia Soil Penetration Experiment at DRES: Results and Analysis", Sandia Laboratory Report SAND 75-0001, March 1975.

10. Personal Communication, California Research & Technology, Inc.

APPENDIX: THE SLA CAP MODEL

A. TERMINOLOGY AND GENERAL CAP DESCRIPTION

To avoid confusion and establish our terminology, a discussion of the particular type of cap model under consideration will be given first.

Suppose that a velocity field is defined throughout a material. Let u^i be the contravariant components of the velocity vector. The deformation rate tensor is defined as

$$d_j^i = \frac{1}{2}\left(u_{,j}^i + u_{,i}^j\right) \tag{A-1}$$

and the spin tensor as

$$\omega_j^i = \frac{1}{2}\left(u_{,j}^i - u_{,i}^j\right) \tag{A-2}$$

where the comma denotes covariant differentiation. The stress rate experienced by a material element is given by

$$\hat{t}_j^i = \frac{\partial}{\partial t}\, t_j^i + u^\alpha t_{j,\alpha}^i + t_\alpha^i \omega_j^\alpha - t_j^\alpha \omega_\alpha^i \tag{A-3}$$

where we have employed the Jaumann-Noll definition of stress rate,* and t_j^i are the components of the stress tensor. We shall adopt the point of view that the stress rate experienced by a material element in the absence of spin is

$$\frac{Dt_j^i}{Dt} = \frac{\partial t_j^i}{\partial t} + u^\alpha t_{j,\alpha}^i = C_j^i\left(d_\ell^k\right) \tag{A-4}$$

where C_j^i is a tensor function of the deformation rate. In this note, we will use an incremental form of Hooke's Law, which is, however,

---

*Prager, W., "An Elementary Discussion of Definitions of Stress Rate," Quarterly Journal of Applied Mathematics, 18, 1961, p. 403.

considerably different from that associated with the classical Hooke's Law commonly used in static linear elasticity. The incremental Hooke's Law is based on the assumption that

$$dt^i_j = \lambda d\epsilon^\alpha_\alpha \delta^i_j + 2G \, d\epsilon^i_j \tag{A-5}$$

is the law governing any small arbitrary deformation from the current stressed state to a nearby neighboring state. This law is assumed to be valid even when the body is in a high state of stress, and cannot be considered isotropic any longer. Truesdell* has shown that Equation (A-5) is equivalent to

$$\frac{Dt^i_j}{Dt} = \lambda d^\alpha_\alpha \delta^i_j + 2G \, d^i_j \tag{A-6}$$

The cap model assumes that the total deformation rate may be written as the sum of an elastic and a plastic deformation rate:

$$d^i_{j_T} = d^i_{j_e} + d^i_{j_p} \tag{A-7}$$

and that the stress rate depends only upon $d^i_{j_e}$, the elastic component. It is common to define a failure locus, $F_1(t^i_j) = 0$, which is fixed in stress space, and a movable yield locus, called a cap, as $F_2(t^i_j, \kappa) = 0$. The "hardening parameter", κ, is usually defined to be a function of the plastic deformation. The spin terms in Equation (A.3) cause the stress tensor to vary with time, even though the deformation rates might be zero. To avoid difficulties from this source, F_1 and F_2 are usually defined to be functions of the invariants of the stress tensor, which are not altered by the spin terms. The invariants usually used for this purpose are t^i_i and $t^i_j{}^* t^j_i{}^*$, where $t^i_j{}^*$ is the deviator of the stress tensor, defined by

$$t^i_j{}^* = t^i_j - \frac{1}{3} t^\alpha_\alpha \delta^i_j \tag{A-8}$$

---

*Truesdell, C., "The Mechanical Foundations of Elasticity and Fluid Dynamics," Journal of Rational Mechanics and Analysis, 1, 1952, p. 220.

40

When the stress state attains either of the loci, and attempts to pass beyond it, a plastic deformation arises which maintains the stress state on the locus. In the case of the failure surface, the locus remains fixed, and the stress state in general moves along it, but may also remain fixed. In the case of the cap, the existence of the plastic deformation rate causes the cap locus to change, and the stress state moves in such a manner as to stay on the cap.

To complete the specification, a flow rule is required. If the associated flow rule is used, it specifies that

$$d_{j_p}^i = \Lambda \frac{\partial F}{\partial t_j^i} \tag{A-9}$$

where Λ is a scalar which is determined by the simultaneous application of this rule and those discussed above.

When the deformation rate is such as to carry the stress state back within both loci, the plastic deformation rate is again set to zero.

The use of tensor analysis has permitted this terse and concise description of the cap model. To make the exposition easier to follow and visualize, some simplifying terminology is introduced at this point and will be used in the sequel. For precise work, however, it is always well to revert to the tensor formalism.

Instead of deformation rates, the notion of an increment will be introduced, which may be viewed for example, as

$$d\epsilon_{ij} = d_j^i \, \delta t$$

where δt is a small increment of time. Equation (A-4) will be

41

reduced to the two independent equations

$$\frac{Dt_i^i}{Dt} = \left(\lambda + \frac{2}{3}G\right) d_i^i$$

$$\frac{Dt_j^{i\star}}{Dt} = 2G \, d_j^{i\star}$$

(A.10)

and the corresponding increments are

$$dP = K \, d\epsilon$$

where dP and dϵ are increments in the mean stress and volumetric strain

$$ds_{ij} = 2G \, d\epsilon_{ij}^\star$$

(A.11)

and s_{ij} denotes deviatoric stress components. In expressing the increments, the physical components are used, and compressive stresses and strains will be positive. The Einstein summation convention remains applicable, and is used. When the terms "shear stress" and "shear strain" are used, they will mean the deviatoric components. An apology is made for using the two terms interchangeably in what follows.

The constitutive relations used by SLA to prescribe the stress rate as a function of the elastic deformation rate conforms with the hypo-elastic theory of Truesdell,* and is perfectly consistent with the cap model. In this theory, the stress rate depends on the current stress state, the deformation rate, and the elastic moduli, which may be functions of the invariants of the stress tensor.

---

*Truesdell, C., and R. Toupin, "The Classical Field Theories," Handbuch der Physik, Vol. III/1, Springer-Verlag, 1960, p. 732.

A.1 DESCRIPTION OF THE MODEL

A.1.1 Layers 1, 2 and 3

Both the initial SLA report,[7] and a subsequent correction, contained some slight inaccuracies and omissions in the description of their cap model. To permit a precise discussion, the model is described more completely here.

For layers 1, 2 and 3, the failure locus is prescribed by

$$\tau = A - Ce^{-BP} \tag{A.1-1}$$

This locus is supposed to represent the triaxial shear failure locus prescribed by WES,[2,3] and does not move. In SLA's nomenclature, τ is the octahedral shear stress, defined by

$$\tau = \sqrt{s_{ij}s_{ij}/3} \tag{A.1-2}$$

where s_{ij} are the physical components of the deviatoric stress tensor.

The movable cap is defined by

$$\frac{\tau^2}{\left(\frac{X-L}{R}\right)^2} + \frac{(P-L/\sqrt{3})^2}{\left(\frac{X-L}{\sqrt{3}}\right)^2} = 1 \tag{A.1-3}$$

where we have cast the original expression into the classical form for an ellipse. The quantities X and L vary with the plastic volumetric strain, ε_p, but R is constant for a given layer. The ellipse is centered at $\tau = 0$, $P = L/\sqrt{3}$. The semi-axis in the τ direction has length $(X-L)/R$, and that in the P direction has length $(X-L)/\sqrt{3}$.

The intersection of the cap with the p-axis is at $P_v = X/\sqrt{3}$. This information is summarized in Figure A.1a.

The quantity, L, is prescribed such that the top of the semi-axis in the τ direction is on the failure locus. This condition leads to

$$\frac{X-L}{R} = A - Ce^{-BL/\sqrt{3}} \tag{A.1-4}$$

Equation (A.1-4) is used only when it leads to values of L greater than or equal to zero, which occurs when X is greater than or equal to R(A-C). For smaller values of X, L is assumed to be zero.

The specification is completed by prescribing X as a function of the volumetric plastic strain, through

$$X = \frac{-\ell n(1 - \epsilon_p/w)}{D} \tag{A.1-5}$$

When ϵ_p is large enough to make $X \geq R(A-C)$, the caps have the character shown in Figure A.1a. For smaller values of ϵ_p, the caps lie entirely under the failure locus, and have semi-axes of lengths X/R and $X/\sqrt{3}$ in the τ and p directions, respectively. This is illustrated in Figure A.1b. As X approaches zero, it is seen that the cap degenerates to a point at the origin.

The bulk modulus is given by

$$K = B_0\left[1 - B_1 e^{-B_2 P}\right] \tag{A.1-6}$$

where B_0, B_1, and B_2 are constant for a given layer. This modulus gives the rate at which pressure increases with elastic volumetric compaction $d\epsilon_e$. That is $K = (\partial P/\partial \epsilon_e)$. If an increment of volumetric compression, $d\epsilon_T$, is applied to the material, and no volumetric plastic strain occurs, then $d\epsilon_e = d\epsilon_T$, and $dP = Kd\epsilon_T$ prescribes the net
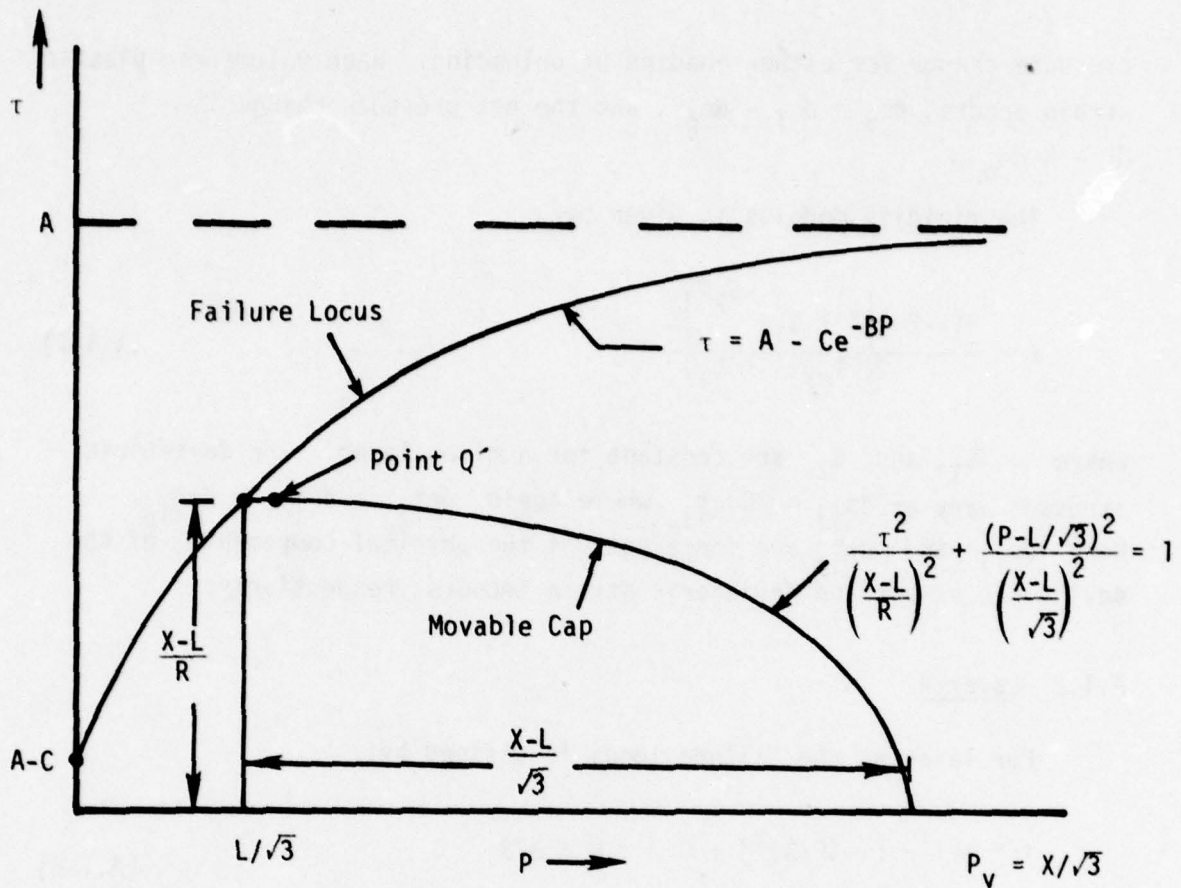
44

Figure A.1a. Cap geometry for layers 1, 2 and 3 when $X \geq R(A-C)$
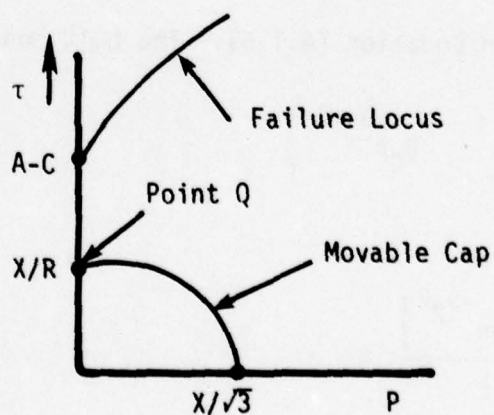
Figure A.1b. Cap geometry for layers 1, 2 and 3 when $X < R(A-C)$.

45

pressure change for either loading or unloading. When volumetric plastic strain occurs, $d\epsilon_e = d\epsilon_T - d\epsilon_p$, and the net pressure change is $dP = K\,d\epsilon_e$.

The rigidity modulus is given by

$$G = \frac{3(1-2\nu)\left[1 + S_1 e^{-S_2 P}\right]K}{2(1+\nu)(1 + S_1)} \qquad (A.1-7)$$

where ν, S_1, and S_2 are constant for a given layer. The deviatoric stresses vary as $ds_{ij} = 2G d\epsilon^*_{ij_e}$, where again $d\epsilon^*_{ij_e} = d\epsilon^*_{ij_T} - d\epsilon^*_{ij_p}$. Here ds_{ij} and $d\epsilon^*_{ij}$ are increments of the physical components of the deviatoric stress and deviatoric strain tensors, respectively.

A.1.2 Layer 4

For layer 4, the failure locus is defined by

$$\tau = A\left[1 - (1-3P/B)^2\right] + C \qquad P < B/3$$
$$\tau = A + C \qquad\qquad\qquad P \le B/3 \qquad (A.1-8)$$

The movable cap is given by

$$\tau = X(\epsilon_p)/\sqrt{6} - P/\sqrt{2} \qquad (A.1-9)$$

where $X(\epsilon_p)$ is given in Equation (A.1-5). The bulk modulus is

$$K = \min\left(B_0 e^{B_2 P/B_1}, \quad B_0 e^{B_2\sqrt{3}}\right) \qquad (A.1-10)$$

The rigidity modulus is

$$G = \frac{3(1-2\nu)\left[1 + S_1 e^{-S_2 P}\right]}{2(1+\nu)(1 + S_1)} K \qquad (A.1-11)$$

46

These moduli are to be used in the same way as K and G in the previous section to compute stress increments from strain increments.

A.2 HYDROSTATIC LOADING

For hydrostatic loading, it is possible to solve for the total strain, the plastic strain, and the elastic strain in closed form. In this section, all the strains are volumetric, that is

ε is the total volumetric strain

ε_e is the elastic volumetric strain

ε_p is the plastic volumetric strain.

Positive values of these parameters will denote compressions.

The relation between pressure and the elastic volumetric strain is specified as

$$dP = K \, d\varepsilon_e = B_0 \left(1 - B_1 e^{-B_2 P} \right) d\varepsilon_e \tag{A.2-1}$$

Equation (A.2-1) may be integrated to obtain

$$B_0 \varepsilon_e = P + \frac{1}{B_2} \ell n \left[\frac{1 - B_1 e^{-B_2 P}}{1 - B_1} \right] \tag{A.2-2}$$

where $\varepsilon_e = 0$ at $P = 0$.

The intersection of the cap and the pressure axis in the τ-p plane is given by

$$P_v = \frac{X(\varepsilon_p)}{\sqrt{3}} = \frac{-\ell n(1 - \varepsilon_p/w)}{\sqrt{3} \, D} \tag{A.2-3}$$

which may also be written as

$$\varepsilon_p = w \left(1 - e^{-\sqrt{3} \, D \, P_v} \right) \tag{A.2-4}$$

48

From Equation (A2-4), it is clear that w is the upper limit of volumetric plastic strain, and is approached at high pressures.

In pure hydrostatic loading, starting from the virgin state, the cap is initially a point, but expands in such a manner that P_v is equal to the pressure, P. Therefore, Equations (A.2-2) and (A.2-4) provide a complete specification of P, ε_e, and ε_p. If one is known, both the others can be computed. It is interesting to note that the ratio between the increments of plastic and elastic volumetric strains is given by

$$\frac{d\varepsilon_p}{d\varepsilon_e} = \sqrt{3} \, D(w-\varepsilon_p^-) \, B_0\left(1-B_1 e^{-B_2 P}\right) \tag{A.2-5}$$

This equation shows very clearly that when ε_p approaches w, the ratio of plastic to elastic strain increment approaches zero, and the elastic strain increment is essentially equal to the total strain increment.

By using the relation

$$d\varepsilon = d\varepsilon_e + d\varepsilon_p \tag{A.2-6}$$

the effective bulk modulus for this loading is readily found to be

$$\frac{dP}{d\varepsilon} = \frac{1}{\frac{1}{K} + \sqrt{3} \, D(w-\varepsilon_p)} \tag{A.2-7a}$$

$$= \frac{1}{\frac{1}{B_0\left(1 - B_1 e^{-B_2 P}\right)} + \sqrt{3} \, Dwe^{-\sqrt{3} \, DP}} \tag{A.2-7b}$$

The second term in the denominator of Equations (A.2-7a and b) produces an apparent softening of the bulk modulus due to the plastic volumetric compaction. At high pressures, the softening term goes to zero, and the effective bulk modulus approaches the elastic bulk modulus.

49

The relation between the pressure, P, and total volumetric strain, ε, may be obtained in closed form as

$$\varepsilon = \frac{P}{B_0} + \frac{1}{B_0 B_2} \ln\left(\frac{1-B_1 e^{-B_2 P}}{1-B_1}\right) + w\left(1-e^{-\sqrt{3}DP}\right) \qquad (A.2-8)$$

Hydrostatic loading

50

A.3 GENERAL LOADING

A.3.1 Layers 1, 2 and 3

As described in Section A.1, SLA defines a movable cap in the τ-p plane. The motion of the cap depends only on the volumetric plastic strain, ε_p. All the necessary equations will now be derived to determine the stress-strain paths which will be followed on any general loading, as well as to determine all plastic strains produced.

It will aid in visualization to use a vector description of stress increments in the τ-p plane, and to this end, let $\hat{\tau}$ and $\hat{p}$ represent unit vectors in this plane. See Figure A.3-1. The movable cap is prescribed in the form

$$F(P, \tau, \varepsilon_p) = 0 \tag{A.3-1}$$

The specific form selected is

$$\frac{\tau^2}{a^2} + \frac{(P - L/\sqrt{3})^2}{b^2} - 1 = 0 \tag{A.3-2}$$

where a, b, and L depend on ε_p in the manner described in Section A.1. For some reason, SLA elects to define $\tau = \sqrt{s_{ij}s_{ij}/3}$. Others have used $\sqrt{J_2} = \sqrt{s_{ij}s_{ij}/2}$ as a variable. The author's personal preference is $\sqrt{s_{ij}s_{ij}}$. All cases may be treated together by using the general definition

$$\tau = \sqrt{\beta \, s_{ij}s_{ij}} \tag{A.3-3}$$

where β is any positive constant. This leads to

$$\frac{\partial \tau}{\partial s_{ij}} = \frac{\beta s_{ij}}{\tau} \tag{A.3-4}$$

with the obvious precautions to be taken at $\tau = 0$.

51

$①→④$ $d\bar{\sigma}_T$ Total stress increment without plastic strain

$①→③$ $d\bar{\sigma}_e$ Net stress increment including plastic strain

$②→③$ $d\bar{\sigma}_c$ Cap motion in normal direction

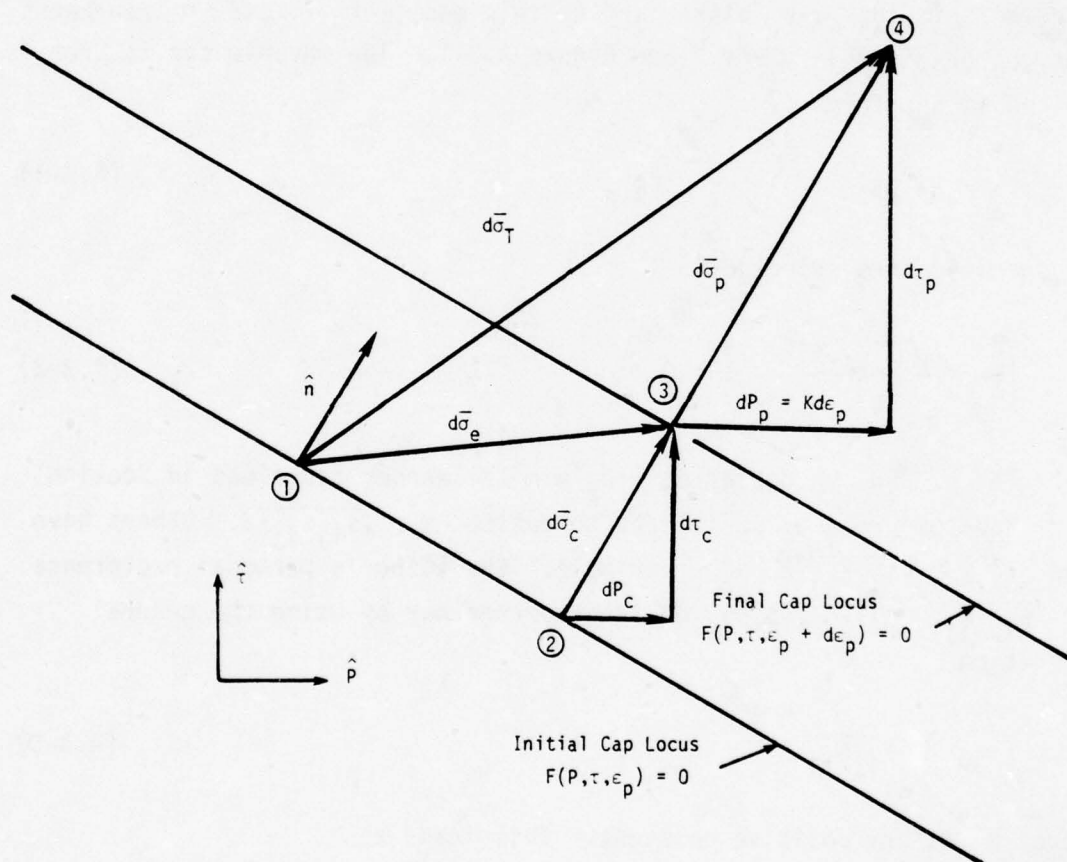$③→④$ $d\bar{\sigma}_p$ Stress diminution due to plastic strain

Figure A.3-1.   Stress increments for a movable cap.

52

The problem to be discussed is: given the incremental strains, $d\epsilon_T$ and $d\epsilon^*_{ij_T}$, find the resulting incremental stresses and plastic strains, according to the SLA model.

As a matter of notation, stresses and strains will be positive in compression, s_{ij} and $d\epsilon^*_{ij}$ are the physical components of the deviatoric stress and strain tensors, and ϵ without indices is the volumetric strain.

The unit vector normal to the cap is

$$\hat{n} = n_p \hat{P} + n_\tau \hat{\tau} \tag{A.3-5}$$

where

$$n_p = \frac{\partial F}{\partial P} \Bigg/ \sqrt{\left(\frac{\partial F}{\partial P}\right)^2 + \left(\frac{\partial F}{\partial \tau}\right)^2}$$

$$n_\tau = \frac{\partial F}{\partial \tau} \Bigg/ \sqrt{\left(\frac{\partial F}{\partial P}\right)^2 + \left(\frac{\partial F}{\partial \tau}\right)^2} \tag{A.3-6}$$

The application of the strains tends to produce the total increments

$$dP_T = K \, d\epsilon$$

$$ds_{ij_T} = 2G \, d\epsilon^*_{ij_T} \tag{A.3-7}$$

Multiplying the i,jth component of Equation (A.3-4) by ds_{ij} and summing, yields using (A.3-7)

$$d\tau_T = \frac{2G\beta}{\tau} \left(s_{ij} \, d\epsilon^*_{ij_T}\right) \tag{A.3-8}$$

Here K and G are the bulk and rigidity moduli, respectively. In the τ-p plane, these contributions tend to create the total stress

53

increment vector

$$d\overline{\sigma}_T = \hat{P}dP_T + \hat{\tau} \, d\tau_T \tag{A.2-9}$$

which extends from point 1 to point 4 in Figure A.3-1. If this vector has a positive outward component, then point 4 falls outside the cap. This is the criterion for plastic strains to occur, which provide the stress reduction shown as $d\overline{\sigma}_p$ in Figure A.3-1. (Note that the increments are considered to be so small that the curvature of the cap may be neglected.) For an isotropic material, the associated flow rule stipulates that $d\overline{\sigma}_p$ shall be normal to the cap. In addition, the cap moves according to some function of the parameters. In the present instance, the motion depends only on $d\varepsilon_p$. This produces a motion of the cap in the normal direction by the amount $d\overline{\sigma}_c$ in Figure A.3-1. The condition that the final stress state at point 3 be on the new location of the cap is embodied in the expression

$$\hat{n}\left(\hat{n} \cdot d\overline{\sigma}_T\right) = d\overline{\sigma}_c + d\overline{\sigma}_p \tag{A.3-10}$$

which closes the system of equations, and permits one to solve for all relevant quantities.

In the case at hand, emphasis is on the volumetric and pressure components, and it is the $\hat{P}$-component of Equation (A.3-10), i.e.,

$$n_p^2 \, dP_T + n_p n_\tau d\tau_T = dP_c + dP_p = dP_c + Kd\varepsilon_p \tag{A.3-11}$$

which proves useful.

There remains only to compute dP_c, the change in pressure which a point moving normal to the cap experiences during the cap migration. This is accomplished by differentiating Equation (A.3-2), the expression for the cap locus:

$$\frac{2\tau d\tau_c}{a^2} + \frac{2(P-L/\sqrt{3})dP_c}{b^2} - \left[\frac{2\tau^2}{a^3}\frac{\partial a}{\partial \varepsilon_p} + \frac{2(P-L/\sqrt{3})^2}{b^3}\frac{\partial b}{\partial \varepsilon_p} + \frac{2(P-L/\sqrt{3})}{\sqrt{3}\,b^2}\frac{\partial L}{\partial \varepsilon_p}\right]d\varepsilon_p = 0$$

$$\tag{A.3-12}$$

54

Since $d\tau_c$ and dP_c must produce a change of the surface in the direction of $\hat{n}$,

$$dr_c = n_\tau dP_c / n_p = \frac{\tau}{a^2} \frac{b^2}{P - L/\sqrt{3}} dP_c \qquad (A.3\text{-}13)$$

which leads to

$$dP_c = \alpha d\epsilon_p \qquad (A.3\text{-}14)$$

where

$$\alpha = \frac{\dfrac{\tau^2}{a^3} \dfrac{\partial a}{\partial \epsilon_p} + \dfrac{(P-L/\sqrt{3})^2}{b^3} \dfrac{\partial b}{\partial \epsilon_p} + \dfrac{P-L/\sqrt{3}}{\sqrt{3}\, b^2} \dfrac{\partial L}{\partial \epsilon_p}}{\dfrac{\tau^2}{a^4} \dfrac{b^2}{P-L/\sqrt{3}} + \dfrac{P-L/\sqrt{3}}{b^2}} \qquad (A.3\text{-}15)$$

From Section A.1, one has

$$a = \frac{X-L}{R} \quad \text{and} \quad b = \frac{X-L}{\sqrt{3}} \quad \text{if} \quad X \ge R(A-C)$$

$$a = \frac{X}{R} \quad \text{and} \quad b = \frac{X}{\sqrt{3}} \quad \text{if} \quad X < R(A-C)$$

$$X = \frac{-\ln(1-\epsilon_p/w)}{D}, \qquad \frac{\partial X}{\partial \epsilon_p} = \frac{1}{D(W-\epsilon_p)} \qquad (A.3\text{-}16)$$

since L satisfies Equation (A.1-4)

$$\frac{\partial L}{\partial \epsilon_p} = \frac{\partial X}{\partial \epsilon_p} \Bigg/ \left(1 + \frac{RCB}{\sqrt{3}} e^{-BL/\sqrt{3}}\right)$$

which completes the specifications necessary to evaluate Equation (A.3-15).

55

The plastic volumetric strain increment may now be found from Equation (A.3-11) as

$$d\epsilon_p = \left(n_p^2 \, dP_T + n_p n_\tau \, d\tau_T\right)/(\alpha + K) \qquad (A.3-17)$$

The reduction in stress due to plastic strains are:

$$dP_p = Kd\epsilon_p$$

$$d\tau_p = n_\tau dP_p/n_p \qquad (A.3-18)$$

Therefore, the net stress increments are

$$dP_e = dP_T - dP_p = K(d\epsilon_T - d\epsilon_p)$$

$$d\tau_e = d\tau_T - d\tau_p \qquad (A.3-19)$$

When a plastic increment in τ occurs, plastic increments of deviatoric strain are produced, whose magnitudes are governed by the associated flow rule,

$$d\epsilon_{ij_p}^* = \lambda \, \frac{\partial F}{\partial \tau} \frac{\partial \tau}{\partial s_{ij}} = \lambda s_{ij} \qquad (A.3-20)$$

These create the increment $d\tau_p$ in accordance with

$$d\tau_p = \frac{\partial \tau}{\partial s_{ij}} 2Gd\epsilon_{ij_p}^* = \frac{2G\lambda\beta \, s_{ij}s_{ij}}{\tau} = 2G\lambda\tau \qquad (A.3-21)$$

Therefore

$$\lambda = \frac{d\tau_p}{2G\tau}$$

and

$$d\epsilon_{ij_p}^* = \frac{d\tau_p}{\tau} \frac{s_{ij}}{2G} \qquad (A.3-22)$$

56

The net increment in the components of deviatoric stress are therefore given by

$$ds_{ij_e} = ds_{ij_T} - 2Gd\epsilon^*_{ij_p} = ds_{ij_T} - \frac{d\tau_p}{\tau} s_{ij} \qquad (A.3-23)$$

These increments must now be adjusted to reflect the effects of the spin tensor of Equation (A-3). The spin tensor does not change τ and P.

A.3.2 Layer 4

For layer 4, the movable cap is defined by the equation

$$F(\tau, P, \epsilon_p) = 0 \qquad (A.3-24)$$

where

$$F = \tau + P/\sqrt{2} - X/\sqrt{6} \qquad (A.3-25)$$

The parameter, X is again

$$X = \frac{-\ln(1 - \epsilon_p/w)}{D}$$

The unit normal vector to $F = 0$ is now constant, having components

$$n_p = \frac{1}{\sqrt{3}}$$

$$\qquad (A.3-26)$$

$$n_\tau = \sqrt{\frac{2}{3}}$$

The considerations shown in Figure A.3-1 are still valid, as are Equations (A.3-7) to (A.3-11), (A.3-14), and A.3-18) to (A.3-23).

57

By analogous mathematics, one is led to

$$dP_p = \frac{\sqrt{3} \, DK(w-\epsilon_p)(dP_T + \sqrt{2} \, d\tau_T)}{1 + 3\sqrt{3} \, DK(w-\epsilon_p)}$$ (A.3-27)

$$d\tau_p = \frac{\sqrt{6} \, DK(w-\epsilon_p)(dP_T + \sqrt{2} \, d\tau_T)}{1 + 3\sqrt{3} \, DK(w-\epsilon_p)}$$ (A.3-28)

The net changes in stress are

$$dP_e = dP_T - dP_p$$ (A.3-29)

$$d\tau_e = d\tau_T - d\tau_p$$ (A.3-30)

58

A.4 DISCUSSION OF THE MODEL

A serious difficulty with the model is that it is neutrally stable to loading in pure shear at certain points in the τ-p plane. One instance of this phenomenon arises in loading from the virgin state. If a pure deviatoric strain increment is applied to the material in that state, no stress whatsoever results. The material could accept an infinite shearing strain, and never depart from the stress state, $P = \tau = 0$.

Even if one assumes a small ε_p in the virgin state, so that the cap becomes a small ellipse, the difficulty still occurs at the top of the cap, for example at point Q in Figure A.1b. Incremental deviatoric strains applied to the material at point Q would result in no incremental stress, and no increment of ε_p to cause the cap to migrate. Again, an infinite shear strain could be accepted by the material without altering the stress state, and in so doing, the material would accept an infinite amount of plastic work.

When the cap grows to the point where it contacts the failure locus, the troublesome point falls on the failure locus, and the problem can be partially alleviated by assuming the failure locus to have precedence. However, points on the cap near its apex (such as point Q´ in Figure A.1a) can still accept very large deviatoric strains, and a very large amount of plastic work, while producing a very small stress increment.

One way to remove this troublesome feature is to specify that the cap locus depends on the deviatoric plastic strain, for example on the generalized plastic strain $d\varepsilon_{ij_p}^* \, d\varepsilon_{ij_p}^*$.

The cap model, at points where the cap is not vertical or horizontal in the τ-p plane, has the property of producing a volumetric plastic strain upon the application of a pure shearing strain, and a deviatoric plastic strain upon the application of a pure volume strain.

59

This is illustrated in the following sketches, which are special cases of Figure A.3-1.

$$d\tau_T = \frac{2G\beta}{\tau} s_{ij}\, d\varepsilon^*_{ijT}$$

$$dP_T = Kd\varepsilon$$
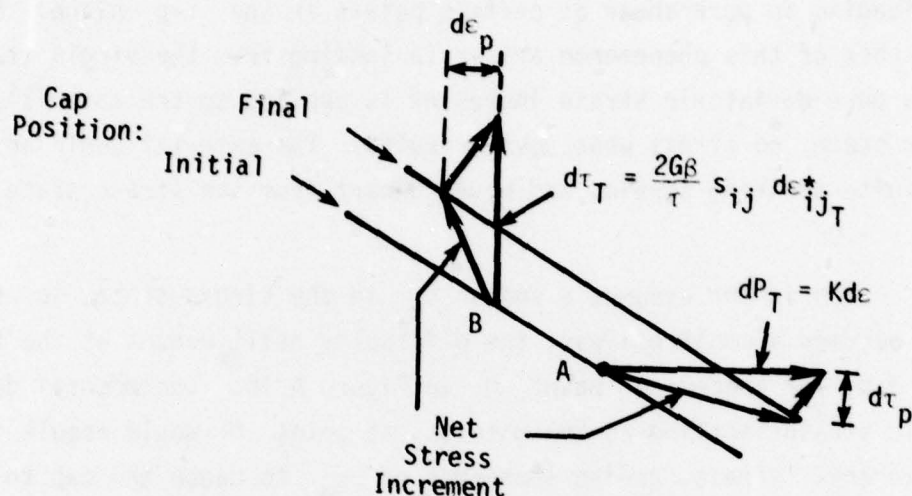
Application of the volumetric strain, $d\varepsilon$, is illustrated at point A, and that of pure deviatoric strains, $d\varepsilon^*_{ijT}$, at point B. For any particular instance, the quantitative increments can be found from the equations of Section A.3. The sketch shows that the plastic strains produced tend to reduce the pre-existing pressure or shear stress. Even if the slope of the cap is of the opposite sign, the shear stress is still reduced by the plastic strain associated with volumetric expansion if the cap expands outward. Of course, mixed loadings produce an appropriate mixture of these results. These considerations illustrate that the detailed geometry of the cap exerts an important influence on the magnitudes of such changes, and a great deal of information is necessary to specify the geometry of the cap correctly. In many instances, such as the case at hand, the geometry is arbitrarily selected to be some simple, easily treated configuration, such as an ellipse, rather than to reflect any knowledge of how the material actually behaves.

60

The cap of layer 4 is assumed to be a straight line, specified by Equation A.3-25. The above sketch has illustrated that a cap of negative finite slope produces a decrement of shear stress upon application of a volumetric compression. A logical question to ask is how this can be so at the point where the cap intersects the p-axis. To avoid this difficulty, one usually insists that the cap be vertical at this intersection. In the present instance, an additional specification* was made to the effect that if the shear stress is zero, and pure volumetric loading occurs, the normal to the cap is to be taken in the direction of the p-axis, and no plastic shear strain is permitted.

However, as the following sketch illustrates, there is a critical angle, θ, for a point on the p-axis. If an incremental strain tends to produce a total incremental stress within this angle, a strict interpretation of the model would lead to the creation of a negative τ, which is impossible.
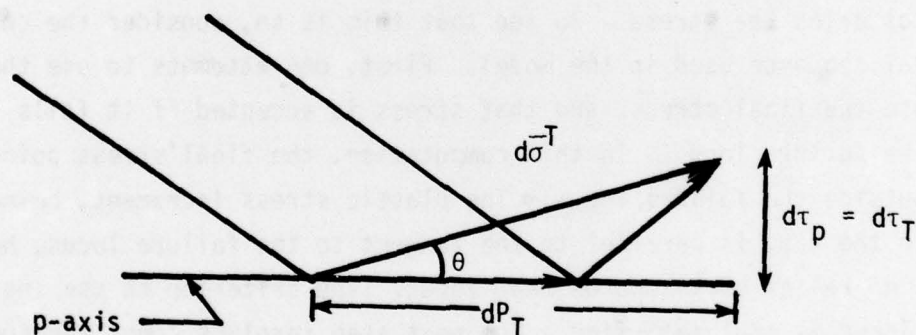
It is seen that the angle, θ, is defined by the condition that

$$d\tau_p = d\tau_T .\qquad\qquad\text{(A.4-1)}$$

---

*Byers, personal communication.

61

Equation (A.3-28) may be used to determine that

$$\tan\theta = \frac{d\tau_T}{dP_T}\Bigg|_{crit} = \frac{\sqrt{6}\ DK(w-\epsilon_p)}{1 + \sqrt{3}\ DK(w-\epsilon_p)} \tag{A.4-2}$$

The constitutive relations are therefore undefined for incremental strains which produce incremental total stresses within the angle, θ.

Another shortcoming of the straight-line cap is that it fails to control the dilatancy in unloading on the failure locus. To demonstrate this, we shall consider a specific example of unloading which can produce unlimited dilatancy. The straight line cap has a constant slope of -3 in the τ-p plane. Consider the point on the failure locus which has a slope of 1/3, and so is normal to the cap. If the stress is at that point, and one applies an incremental strain which tends to produce an incremental total stress with slope -3 (that is $d\tau_T/dP_T$=-3), then all the incremental strain is taken up as plastic strain, and the stress point will remain fixed. Continued straining of this sort will lead to unlimited volumetric plastic strain without altering the stress. To see that this is so, consider the cal-culational sequence used in the model. First, one attempts to use the cap to compute the final stress, and that stress is accepted if it falls within the failure locus. In this computation, the final stress point is always outside the failure locus. The plastic stress increment, being normal to the cap, is parallel to the tangent to the failure locus, hence provides no relief back towards that locus. The criterion to use the failure locus is thus satisfied. The next step involves computing the stress increment using the failure locus, which leads to no stress change. The total stress increment is normal to the failure locus, so that the plastic stress increment is in the same direction as the total stress increment. Thus, there is no component of elastic stress increment tangent to the failure locus. The only solution is to have the stress point remain fixed in its position on the failure locus, which implies that all the strain is taken up as plastic strain. No real material can behave in this manner, undergoing an unlimited expansion without changing stress.

During a process of this sort, the generation of volumetric plastic strain can cause the cap to migrate a large distance from the stress point. If, at some time, the loading is changed so that the cap should be used, the relaxation to the cap occurs instantly, by what may be a very large amount. This violates the principle of continuity, because the stress increment which just causes the cap to be used instead of the failure locus, differs by only a small amount from that which just causes the failure locus to be used. However, the difference in plastic strain between the two cases can be enormous.

DISTRIBUTION LIST

DEPARTMENT OF DEFENSE

Assistant to the Secretary of Defense
Atomic Energy
    ATTN: Executive Assistant

Defense Advanced Rsch. Proj. Agency
    ATTN: TIO

Defense Civil Preparedness Agency
    ATTN: Hazard Eval. & Vul. Red. Div., G. Sisson

Defense Documentation Center
12 cy ATTN: DD

Defense Intelligence Agency
    ATTN: DT-2
    ATTN: DB-4C, E. O'Farrell
    ATTN: RDS-3A
    ATTN: DB-4E

Defense Nuclear Agency
    ATTN: DDST
    ATTN: SPAS
4 cy ATTN: TITL
5 cy ATTN: SPSS

Field Command
Defense Nuclear Agency
    ATTN: FCPR

Field Command
Defense Nuclear Agency
    ATTN: FCPRL

Interservice Nuclear Weapons School
    ATTN: TTV

Joint Strat. Tgt. Planning Staff
    ATTN: NRI-STINFO Library

NATO School (SHAPE)
    ATTN: U.S. Documents Officer

Under Secy. of Def. for Rsch. & Engrg.
    ATTN: Strategic & Space Systems (OS)

DEPARTMENT OF THE ARMY

Chief of Engineers
Department of the Army
2 cy ATTN: DAEN-MCE-D
2 cy ATTN: DAEN-RDM

Deputy Chief of Staff for Ops. & Plans
Department of the Army
    ATTN: MOCA-ADL
    ATTN: DAMO-NC

Deputy Chief of Staff for Rsch. Dev. & Acq.
Department of the Army
    ATTN: DAMA-CSS-N, N. Barron

Engineer Studies Center
Department of the Army
    ATTN: DAEN-FES

DEPARTMENT OF THE ARMY (Continued)

Gator Mine Program
Department of the Army
    ATTN: E. Lindsey

Harry Diamond Laboratories
Department of the Army
    ATTN: DELHD-N-P
    ATTN: DELHD-N-P, J. Gwaltney

U.S. Army Armament Material Readiness Command
    ATTN: MA Library

U.S. Army Ballistic Research Labs
    ATTN: DRDAR-BLT, G. Roecker
    ATTN: DRDAR-BL
    ATTN: DRDAR-BLT
    ATTN: DRDAR-BLT, A. Ricchiazzi
    ATTN: DRDAR-BLE, J. Keefer
    ATTN: DRDAR-BLT, G. Grabarek
2 cy ATTN: DRDAR-TSE-S

U.S. Army Cold Region Res. Engrg. Lab.
    ATTN: G. Swinzow

U.S. Army Comb. Arms Combat Dev. Acty.
    ATTN: G. Steger

U.S. Army Engineer Center
    ATTN: ATZA

U.S. Army Engineer Div. Huntsville
    ATTN: HNDED-SR

U.S. Army Engineer Div. Missouri River
    ATTN: Technical Library

U.S. Army Engineer School
    ATTN: ATZA-CDC
    ATTN: ATZA-DTE-ADM

U.S. Army Engr. Waterways Exper. Station
    ATTN: G. Jackson
    ATTN: D. Butler
    ATTN: W. Flathau
    ATTN: J. Strange
    ATTN: L. Ingram
    ATTN: Library
    ATTN: B. Rohani

U.S. Army Mat. Cmd. Proj. Mngr. for Nuc. Munitions
    ATTN: DRCPM-NUC

U.S. Army Material & Mechanics Rsch. Ctr.
    ATTN: Technical Library

U.S. Army Materiel Dev. & Readiness Cmd.
    ATTN: DRXAM-TL

U.S. Army Materiel Sys. Analysis Activity
    ATTN: DRXSY-D, J. Sperrazza

U.S. Army Missile R&D Command
    ATTN: W. Jann
    ATTN: F. Fleming
    ATTN: RSIC

DEPARTMENT OF THE ARMY (Continued)

U.S. Army Mobility Equip. R&D Cmd.
    ATTN: DRDDME-XS
    ATTN: DRDME-WC

U.S. Army Nuclear & Chemical Agency
    ATTN: Library

U.S. Army War College
    ATTN: Library

DEPARTMENT OF THE NAVY

Marine Corps
Department of the Navy
    ATTN: POM

Marine Corp Dev. & Education Command
Fire Support Section
    ATTN: D091, J. Hartneady

Naval Air Systems Command
    ATTN: F. Marquardt

Naval Construction Battalion Center
Civil Engineering Laboratory
    ATTN: Code L51, R. Odello
    ATTN: Code L08A

Naval Explosive Ord. Disposal Fac.
    ATTN: Code 504, J. Petrousky

Naval Facilities Engineering Command
    ATTN: Code 09M22C

Naval Postgraduate School
    ATTN: Code 0142

Naval Research Laboratory
    ATTN: Code 2627

Naval Sea Systems Command
    ATTN: Sea-9931G
    ATTN: SEA-033

Naval Surface Weapons Center
    ATTN: Code X211
    ATTN: Code F31
    ATTN: Code U401, M. Kleinerman

Naval Surface Weapons Center
    ATTN: Tech. Library & Info. Services Branch

Naval Weapons Center
    ATTN: Code 266, C. Austin
    ATTN: Code 233

Naval Weapons Evaluation Facility
    ATTN: Code 10

Office of Naval Research
    ATTN: Code 715

Office of the Chief of Naval Operations
    ATTN: OP 982E, M. Lenzini
    ATTN: OP 982
    ATTN: Code 604C3, R. Piacesi

Strategic Systems Project Office
Department of the Navy
    ATTN: NSP-43

DEPARTMENT OF THE AIR FORCE

Air Force Armament Laboratory
    ATTN: ADTC/XRS, M. Valentine
3 cy ATTN: DLYV, J. Collins

Air Force Institute of Technology
    ATTN: Library

Air Force Weapons Laboratory, AFSC
    ATTN: SUL

Assistant Chief of Staff, Intelligence
    ATTN: INT

Deputy Chief of Staff
    ATTN: R. Steere

Foreign Technology Division, AFSC
    ATTN: NIIS Library

Oklahoma State University
Fld. Off. for Wpns. Effectiveness
    ATTN: E. Jackett

Rome Air Development Center, AFSC
    ATTN: TSLD

Space & Missile Systems Organization
Air Force Systems Command
    ATTN: RSS

DEPARTMENT OF ENERGY

Department of Energy
Albuquerque Operations Office
    ATTN: CTID

Department of Energy
    ATTN: Classified Library
    ATTN: OMA/RD&T Test Office

Department of Energy
Nevada Operations Office
    ATTN: Technical Library

OTHER GOVERNMENT AGENCIES

NASA
Ames Research Center
    ATTN: R. Jackson

U.S. Nuclear Regulatory Commission
    ATTN: L. Shao

DEPARTMENT OF ENERGY CONTRACTORS

Sandia Laboratories
    ATTN: 3141
    ATTN: W. Herrmann
    ATTN: J. Colp
    ATTN: A. Chabai
    ATTN: W. Altsmeirer
    ATTN: W. Patterson
    ATTN: J. Keizur
    ATTN: W. Caudle

Lawrence Livermore Laboratory
    ATTN: L-504, M. Wilkins
    ATTN: Technical Information Dept. Library
    ATTN: J. Goudreau

DEPARTMENT OF ENERGY CONTRACTORS (Continued)

Los Alamos Scientific Laboratory
    ATTN: MS 364
    ATTN: T. Dowler

Sandia Laboratories
    ATTN: Library & Security Classification Div.

DEPARTMENT OF DEFENSE CONTRACTORS

Aerospace Corp.
    ATTN: Technical Information Services

Agbabian Associates
    ATTN: M. Agbabian

Applied Theory, Inc.
 2 cy ATTN: J. Trulio

AVCO Research & Systems Group
    ATTN: D. Henderson
    ATTN: Library
    ATTN: P. Grady

BDM Corp.
    ATTN: T. Neighbors
    ATTN: Corporate Library

Boeing Co.
    ATTN: Aerospace Library

California Research & Technology, Inc.
    ATTN: K. Kreyenhagen
    ATTN: Library

Civil Systems Inc.
    ATTN: J. Bratton

EG&G Washington Analytical Services Center, Inc.
    ATTN: Library

General Dynamics Corp.
    ATTN: K. Anderson

General Electric Co.-TEMPO
    ATTN: DASIAC

Georgia Institute of Technology
Georgia Tech. Research Institute
    ATTN: L. Rehfield
    ATTN: S. Hanagud

Honeywell, Inc.
Defense Systems Division
    ATTN: T. Helvig

University of Illinois
Consulting Services
    ATTN: N. Newmark
    ATTN: W. Hall

Institute for Defense Analyses
    ATTN: Classified Library

Kaman AviDyne
    ATTN: Library
    ATTN: N. Hobbs
    ATTN: E. Criscione

Weidlinger Assoc., Consulting Engineers
    ATTN: J. Isenberg

DEPARTMENT OF DEFENSE CONTRACTORS (Continued)

Kaman Sciences Corp.
    ATTN: Library

Lockheed Missiles & Space Co., Inc.
    ATTN: M. Culp
    ATTN: TIC-Library

Lockheed Missiles and Space Co., Inc.
    ATTN: Technical Information Center

Martin Marietta Corp.
    ATTN: H. McQuaig
    ATTN: A. Cowan
    ATTN: M. Anthony

Merritt CASES, Inc.
    ATTN: J. Merritt
    ATTN: Library

University of New Mexico
Dept. of Police & Parking Security
    ATTN: G. Triandafalidis

Pacifica Technology
    ATTN: G. Kent
    ATTN: R. Bjork

Physics International Co.
    ATTN: Technical Library
    ATTN: L. Behrmann

R & D Associates
    ATTN: P. Rausch
    ATTN: J. Lewis
    ATTN: A. Fields
    ATTN: H. Brode
    ATTN: C. MacDonald
    ATTN: Technical Information Center
    ATTN: W. Wright, Jr.

R & D Associates
    ATTN: H. Cooper

Rand Corp.
    ATTN: Library

Science Applications, Inc.
    ATTN: Technical Library

SRI International
    ATTN: J. Colton
    ATTN: G. Abrahamson

Systems, Science & Software, Inc.
    ATTN: Library
    ATTN: R. Sedgewick

Terra Tek, Inc.
    ATTN: Library

TRW Defense & Space Sys. Group
    ATTN: P. Dai
    ATTN: Technical Information Center

TRW Defense & Space Sys. Group
    ATTN: E. Wong

Weidlinger Assoc., Consulting Engineers
    ATTN: M. Baron
    ATTN: J. McCormick